AGN Variability in the UKIDSS Ultra Deep Survey

Elizabeth Helen Elmer, MSci

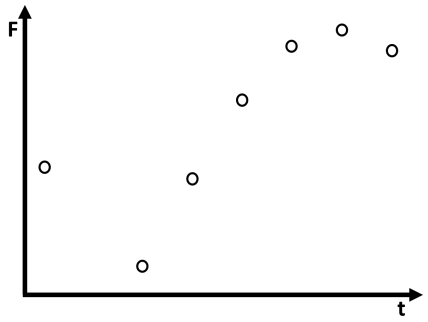

Thesis submitted to the University of Nottingham
for the degree of Doctor of Philosophy

June 2021

"You're braver than you believe, stronger than you seem, and smarter than you think"

– A.A. Milne

Supervisors:	Prof. Omar Almaini	
	Prof. Michael Merrifield	
Examiners:	Prof. Ian McHardy	(University of Southampton)
	Dr. Steven Bamford	(University of Nottingham)
Submitted:	15th June 2021	
Examined:	27th July 2021	
Final version:	19th August 2021	

Contents

List of Tables

List of Figures

Abstract

One of the defining characteristics of Active Galactic Nuclei (AGN) is the variations observed in their fluxes. In this thesis, we present the first attempt to select AGN using long-term near-infrared (NIR) variability. By analysing the K-band light curves of all the galaxies in the UKIDSS Ultra Deep Survey (UDS), the deepest NIR survey over ~ 1 sq degree, we have isolated 393 variable AGN candidates. In order to minimise any contamination, known galactic stars were removed from the catalogue before the selection was run, and we took care to suppress any spurious variations due to atmospheric seeing. A comparison to other selection techniques shows that only half of the variable sources are also selected using either deep Chandra X-ray imaging or IRAC colour selection, suggesting that using NIR variability can locate AGN that are missed by more standard selection techniques. In particular, we find that long-term K-band variability identifies AGN at low luminosities and in host galaxies with low stellar masses, many of which appear relatively X-ray quiet.

We then present how the variability selection can be extended to also select AGN from analysis of the J-band light curves. Through this analysis, we showed that a further population of AGN is found using this bluer waveband. When this new sample is combined with those selected in the K-band, we select a total of 595 variable AGN: 177 of these are selected as variable in both bands, 230 are only variable in the J-band, and 188 are only variable in the K-band. By comparing these three populations of AGN, we discovered that their host galaxies have systematically different properties. In general, those detected as variable in both bands are bright, quasar-like AGN, those selected in J are hosted in bluer galaxies, and the K-band only sample have redder, more passive galaxy colours. In particular, a subset of variables only selected in the K-band have properties consistent with dust-obscured AGN.

Once we had obtained this combined sample of AGN that vary in the NIR, we went on to examine the light curves themselves. Information on the structure around AGN has long been derived from measuring lags in their varying light output at different

wavelengths. In most accretion disk models we predict that the infrared light emerges further from the central black hole than the optical light, potentially even probing reprocessed radiation in any surrounding dusty torus. In practice, this has proved challenging because high quality data are required to detect such variability, and the observations must stretch over a long period to probe the likely month-scale lags in variability. In addition, large numbers of sources would need to be observed to start searching for any patterns in such lags. Here, we show that the UDS, built up from repeated observations over almost a decade, provides an ideal data set for such a study. For 96 sources identified as strongly-varying AGN within its square-degree field, we find that the K-band light curves systematically lag the J-band light curves by an average of around a month. The lags become smaller at higher redshift, consistent with the band shift to optical rest-frame emission. The less luminous AGN also display shorter lags, as would be expected if their physical size scales with luminosity.

Acknowledgements

Firstly, I would like to thank Omar and Mike for all their support and encouragement throughout my PhD. Thank you for always being available for me to ask questions, pushing me to start taking control of my research, supporting me when I took on slightly crazy side projects, and calming me down when I was panicking about something that was 100% under control (e.g. this thesis). I couldn't have asked for more supportive and encouraging supervisors. I'd also like to thank everyone who has been part of the UDS group during my PhD, particularly Dave and Will for answering my many questions about the UDS catalogues and images.

Rachel, you deserve a shout out of your own for all the advice and help you have given me, from before I'd decided to take the PhD right up to putting up with out-of-the-blue thesis updates over Facebook messenger! You helped me stay sane when I was bored of data processing and always made me laugh when things got me down. I'm so glad I got a desk in your office.

Amy, you also get your own mention! I genuinely couldn't have got through this PhD without you, you put up with me constantly coming and distracting you in your office and your friendship has just been amazing throughout. Simon, don't think you got away either, thank you for all the support and for picking me up when I was at some of the lowest points of this whole process.

To Karel and Lizzie T, our newest UDSers, thank you for asking me all the python questions and letting me escape thesis writing for a bit. You are both amazing researchers and I know you are going to do great things. Also, shout out to everyone who has been in B105 with me, thank you for distracting me with crazy conversations and putting up with me swearing at python. I miss you all and I'm so sad that we were deprived of our final year together.

A huge thank you to all the the tea break people (Simon, Amy, Rachel, Jake, Charutha, Miguel, Tom, Roan, Mick, CB, Karel, Kellie and Matt) for helping me keep

up a routine and joining me in rants about whatever had gone wrong that day. Special shout out to those of you who helped me carry this on in lockdown - these chats kept me sane when I hadn't seen any people in months!

Next up, I'd like to thank my pgWiP team (Clare, Amy, Emily and Hannah)! While not directly thesis-related, organising and running the conference was one of the highlights of my PhD and I'm still so proud of us. Special thanks to Clare for wholeheartedly supporting us from day one, and for generally being really supportive and encouraging in all things, not just the conference.

Thank you to everyone who has been a part of UCAS days since I started helping out in my second year of UG. I genuinely wouldn't be where I am today without UCAS days, they have given me so much confidence in myself and in public speaking, so thank you to Phil, Meghan, Jules and Pauline for employing and supporting me for all those years! I would also like to thank Chris and Hannah for your friendship and support, I miss camping out in C19, and Charlotte and Emma for our extended lunch breaks and long chats. Actually, just a general shout out to everyone in UoN Physics. I will maintain for a very long time that there is something very special about UoN Physics.

Massive thank you to my family for their support and encouragement that has got me to where I am today. To my sisters for our long video chats and all the sensible advice, and to my mum and dad for always believing I could do anything I set my mind to. I love you all so much.

And last, but definitely not least, the biggest thank you goes to my amazing girlfriend, Sophie. You have been incredible, you are my rock and this thesis would not be anywhere near as good without you. Thank you for putting up with my stresses and reminding me that I could do this all those times I almost gave up. I can't thank you enough.

Published Works

I **Elmer E.**, Almaini, O., Merrifield, M., Hartley, W. G., Maltby, D. T., Lawrence, A., Botti, I., Hirst, P., 2020, MNRAS, 493, 2: *'Long-term NIR variability in the UKIDSS Ultra Deep Survey: a new probe of AGN activity at high redshift'*.

II **Elmer E.**, Merrifield M., Almaini, O., Hartley, W. G., Maltby, D. T., 2021, MNRAS: Letters, 503, 1: *'Infrared lags in the light curves of AGN measured using a deep survey'*.

Chapters 2 and 3 are based on material published in Paper I and Chapter 5 is based on that in Paper II.

The vast majority of the work presented in this thesis was performed by the author, with advice from the paper co-authors listed above. Where the material presented is the result of more collaborative work, this is credited appropriately.

Chapter 1

Introduction

The study of Active Galactic Nuclei (or AGN) has been a rapidly growing area since the late 20th century, although the phenomena associated had been observed as far back as 1909 (Fath, 1909). The term "active galactic nucleus" or "active galaxy" refers to a galaxy where the nucleus is extremely bright, and this brightness is thought to be caused by a black hole at the centre of the galaxy actively accreting matter.

AGN are a particularly interesting area of research as they are some of the most extreme astrophysical environments. Studying how AGN evolve over a range of luminosities, redshifts, and wavelengths can provide insights into how the universe evolved, how galaxies have evolved, and how accretion onto a black hole actually works.

In this introduction, we will summarize our current understanding of AGN, while indicating the developments that led to this knowledge. We start with a general introduction to AGN before moving on to discuss the particular focus of this thesis: AGN variability.

1.1 General Introduction to AGN

Black holes (BHs) are regions of space-time from which nothing can escape, not even light, and their existence has been hypothesized for hundreds of years. The idea that there are regions where light would be unable to escape was initially presented in Mitchell (1784). Mitchell used Newtonian physics to show that, if a star was sufficiently dense and large, its escape velocity would be greater than the speed of light. However, at this time, it was thought that light was made up of particles rather than waves. In the early nineteenth century, it became clear the light had wave-like behaviours and therefore interest in BHs waned as it was thought that light waves would not be affected by gravitational pull.

It was not until Einstein developed his theory of general relativity (Einstein, 1916), and showed that light is affected by gravity, that BHs once again became an interesting area of study. The field equations in Einstein's work were solved later the same year by Karl Schwarzschild, who showed that there was a radius within which light could not escape (Schwarzschild, 1916). However, the nature of the Schwarzschild surface was not understood until 1958, when David Finkelstein described it as an event horizon (Finkelstein, 1958), and the term "black hole" was not used until the late 20th century.

Black holes come in a wide range of sizes, from solar-mass black holes up to the super-massive black holes (SMBHs) that are thought to be at the centre of most galaxies. Extensive optical monitoring of the centre of our galaxy has allowed the orbits of stars to be accurately measured, and these results show that there is, indeed, an invisible mass affecting these orbits (e.g. Gillessen et al., 2009). This monitoring started in the early 1990s and has been continuing ever since, and these results were awarded the 2020 Nobel Prize in Physics. Similar patterns have been seen in other galaxies, suggesting that a SMBH is a common feature of galaxies.

Figure 1.1: The first image of the event horizon around the BH at the centre of M87. The image was released by the Event Horizon Telescope Collaboration in April 2019 (The Event Horizon Telescope Collaboration et al., 2019)

In recent years, there has been a wealth of observational evidence for black holes, including the orbital measurements described above. The recent Event Horizon Telescope (EHT) image of the BH at the centre of M87 (Figure 1.1, The Event Horizon Telescope Collaboration et al., 2019) was one of the most compelling and impressive pieces of evidence. In addition, the first detection of gravitational waves using LIGO (Abbott et al., 2016), followed by the first detection of their electromagnetic counterparts (Abbott et al., 2017), have confirmed Einstein's predictions.

In the mid 20th century, interest was also growing in a class of galaxies with unusual properties. Seyfert (1943) showed that there were strong, broad emission lines in the nuclei of six galaxies, which became known as "Seyfert galaxies", but this discovery went largely unnoticed until Baade & Minkowski (1954) realised that these spectra were similar to the spectrum of the bright Cygnus A radio source. Schmidt (1963) then showed

that 3C 273 was a stellar-like radio object but at a redshift of 0.16, and objects like this became known as quasi-stellar radio sources or "quasars"[1]. Although stellar-like radio sources had been discovered before this, these had been dismissed as stars within our galaxy. In the following years, more quasars were identified with higher redshifts and it was understood that they are the extremely bright nuclei of active galaxies, which is why they became known as active galactic nuclei or AGN. As our understanding of quasars developed, it became clear that Seyfert galaxies were less luminous quasars, where the nucleus does not outshine the galaxy and therefore they are not stellar-like. The AGN have high excitation emission lines that cannot be related to stellar processes, which are now accepted to be due to the presence of a SMBH that is actively accreting matter at the centre of these galaxies.

1.1.1 Structure of AGN

While there are many different observed types of AGN (see Padovani et al., 2017, for a summary table), it is thought that all AGN have the same basic structure and the differences in the observed features is largely due to the observation angle. This is known as the unified model of AGN and was first presented in Antonucci (1993). The model suggests that AGN are made up of an accretion disk, a hot corona of relativistic electrons around the accretion disk, gas clouds that create broad emission lines in the spectra, a torus of obscuring dust, and sometimes relativistic jets. A schematic of this model is shown in Figure 1.2, and Figure 1.3 shows how the emission across the electromagnetic spectrum is thought to relate to particular regions of the AGN.

Accretion disks are found in a wide variety of astronomical objects, including protostars, X-ray binaries, and other binary stars, and are associated with efficient

[1]While historically "quasar" only referred to bright radio AGN, in this thesis the term is used for all bright AGN.

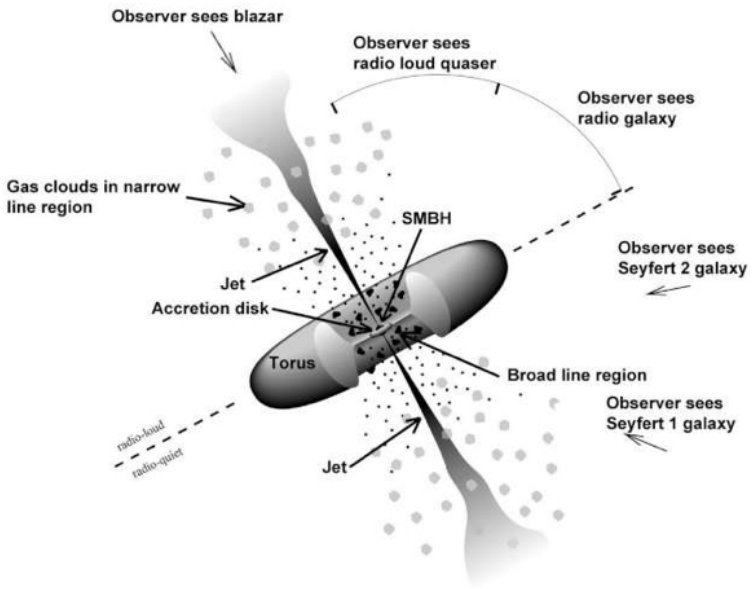

Figure 1.2: Schematic of the unified model of AGN, taken from Beckmann & Shrader (2012). This shows the main features of the AGN that thought to explain the characteristics we observe. It also indicates how the viewing angle can influence the type of AGN observed. "Seyfert 1" and "Seyfert 2" galaxies here are the same as "Type I" and "Type II" AGN.

accretion processes. The accretion disk is the main energy source in an AGN and is largely responsible for determining its observational characteristics. The disk forms when gas falls into the centre of the galaxy while maintaining its angular momentum. The viscosity of the disk then dissipates that momentum, causing the gas to spiral towards the central SMBH. The gravitational energy lost is then transferred into electromagnetic radiation, causing the large luminosities we observe (Netzer, 2013). AGN accretion disks are thought to be optically thick (i.e. they have a high column or surface density) and geometrically thin, and they are observationally evident in the "big blue bump" of the AGN SED in the optical/UV wavebands (Figure 1.3). It should be noted that accretion disk physics is not settled as it is considered by some to be too simplistic to explain phenomena such as extreme variability (Lawrence, 2018).

The X-ray emission from AGN is thought to originate from a hot corona above

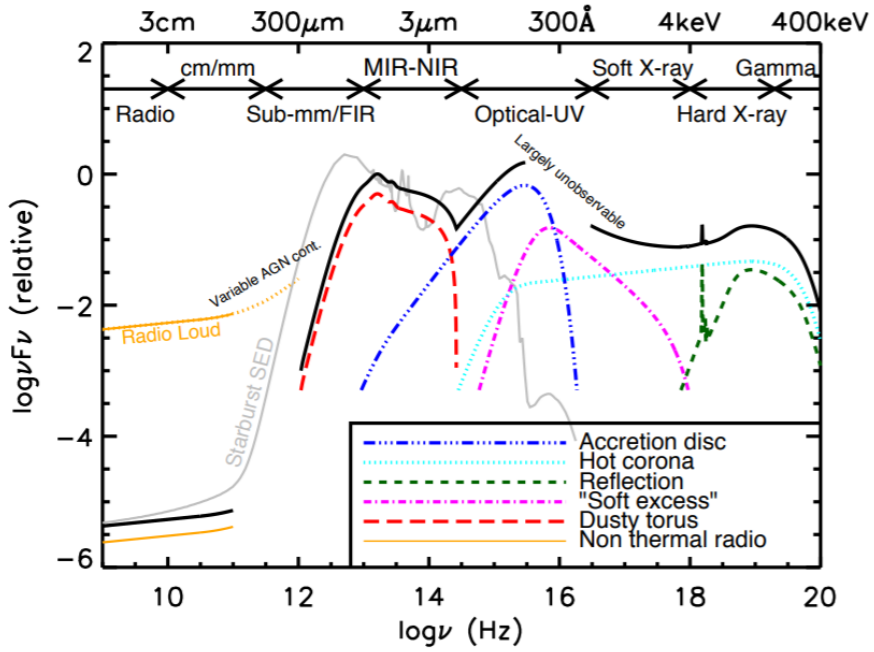

Figure 1.3: A schematic representation of an AGN Spectral Energy Distribution (SED), taken from Harrison (2014). The black solid line represents the total emission, while the coloured lines indicate how each region of the AGN contributes to this overall SED.

and below the accretion disk. The photons emitted from the disk are inverse Compton scattered by relativistic electrons in this envelope of gas, driving the emission to change from optical/UV to X-ray wavelengths. This model also explains the power-law shape of the X-ray spectra of AGN, as the spectral emissivity from inverse Compton scattering is proportional to the photon frequency (e.g. Blumenthal & Gould, 1970).

Surrounding the accretion disk and X-ray corona, in the region known as the "broad line region" (BLR), there are gas clouds that are gravitationally bound to the SMBH. These clouds move at high speeds, and hence emission lines from this region are broad. In addition, the emission lines from this region are permitted lines, which suggests that the density is high enough to suppress forbidden lines. There is also a "narrow line region" (NLR) that extends beyond the gravitational influence of the BH, where the emission lines are narrow as they are not broadened by the movements of the gas clouds.

Spectra from this region also show forbidden emission lines, suggesting it has a lower density then the BLR. In order to "unify" the different types of AGN, in particular the type I (broad line) AGN and type II (narrow line) AGN, it is thought that the BLR is surrounded by a torus of dust that blocks the BLR from view if the AGN is observed from certain angles (see Figure 1.2). This torus emits in the infrared (IR) wavebands as the light from the BH and accretion disk heats the dust.

The final component to the unified AGN model is the presence of relativistic jets. These are needed to explain AGN with large radio and gamma-ray luminosities. These originate close to the BH and the variations in the radio/gamma properties can be explained based either on the viewing-angle of the jet or the lack of a jet if there is little or no radiation in these bands.

It should be noted that the internal structure of AGN is not known. Here we have discussed the cartoon unified model of AGN proposed in Antonucci (1993) as this is a useful guide for considering the physical implications of any results. However, observations are generally raising more questions about the model, rather than confirming it (e.g. Lawrence, 2012, 2018).

1.1.2 Finding AGN

There are a number of features that are typical to AGN, which can tell us about their structure and help us identify AGN in the large scale surveys that make up a large proportion of observations in modern Astronomy. As the Spectral Energy Distribution (SED) of AGN emits at all wavelengths (Figure 1.3), which is a unique feature in itself, we can observe and select AGN across the entire EM spectrum. Each waveband allows us to study a different element of the AGN, and selecting in all wavelengths shows us the wide variety of AGN types that exist in the Universe.

While the SED shows that there is emission from AGN in all wavebands, the emission in X-rays is particularly bright (Elvis et al., 1978). In fact, AGN dominate deep X-ray surveys and therefore these surveys can be used to find AGN. Stars are the main contamination source in this selection so, as long as these are identified and removed, deep X-ray imaging provides a relatively clean sample of AGN.

At other wavelengths, selecting AGN becomes more challenging as bright sources are not necessarily AGN. Optical selection of AGN typically uses colour diagnostics, such as the color-color diagrams shown in Figure 4 of Richards et al. (2001) or the $U-B$ definition given in Schmidt & Green (1983). Unfortunately, these diagnostics tend to have a large amount of contamination, and therefore follow up spectroscopy is generally needed to determine if these sources are definitely AGN.

Due to the dip in the SED of AGN at near-infrared (NIR) wavelengths, AGN are not usually selected in this regime. Instead, IR selection tends to occur in the mid-infrared (MIR), and are once again based primarily on colour diagnostics. The exact selection criteria differ depending on the telescope being used (see Padovani et al., 2017, Table 2 for a summary of criteria). Unfortunately, these methods can also be highly contaminated as the colours are not unique to AGN.

Radio observations are also widely used to select AGN, as they are some of the brightest radio sources. There are numerous types of radio AGN, but generally follow up in other wavebands is needed to robustly categorise them (see Padovani et al., 2017, and references therein). The main alternative source of radio emission is supernova remnants, and therefore the main contamination in radio AGN selection comes from star-forming galaxies (e.g. Condon, 1992).

One of the only ways to be certain that we are looking at an AGN is to examine the spectrum of the object, as AGN have some very distinctive features to look for. Exactly

what features you will see will depend on the type of AGN that you are observing. For instance, quasars and type I AGN have particularly distinctive broad emission lines in their spectra. Generally, AGN have significant line emission, due to high excitation transitions within the AGN, but weak emission from the polycyclic aromatic hydrocarbons (PAHs) and hence the PAH lines are used to distinguish AGN from starburst galaxies (Genzel et al., 1998; Laurent et al., 2000; Weedman et al., 2005).

Finally, and most importantly for this thesis, the continuum and line emission from AGN varies over time, and AGN can be selected based on this characteristic. More detail on AGN variability across the electromagnetic spectrum is given in Section 1.2.

1.2 AGN Variability

Variability has been a known feature of AGN since they were first discovered (e.g. Angione, 1973), and studying the light curves of AGN allows us to probe their innermost regions. These scales are almost impossible to resolve with current telescope facilities, although recently the Event Horizon Telescope imaged the event horizon of a black hole for the first time (Figure 1.1 The Event Horizon Telescope Collaboration et al., 2019). However, this can only be used to observe relatively nearby black holes, and therefore AGN variability is still the best way to resolve these inner regions for the majority of black holes.

Information about the emitting regions of AGN can be determined from a light curve of a single waveband. In particular, the emitting region (R) can be related to the characteristic timescale of variability (t_{var}) using

$$R \leq c\Delta t_{var} \tag{1.1}$$

(e.g. Terrell, 1967), as a region larger than this could not produce variability on these timescales because the outer reaches would not be causally connected. As we are probing timescales of years in the majority of this thesis, this implies we are probing a region ~ 0.5 pc from the central black hole. In addition, examining how variability changes at different wavelengths can help develop a more detailed picture of how the internal components of AGN interact. For instance, we know that the timescale for variability increases as the wavelength increases; variations in X-ray light are seen on timescales of minutes to hours, while in the optical wavebands, variability only becomes clear over days to months. This implies that the X-rays are being emitted from a region close to the central black hole, whereas the optical light comes from further out.

If the comparison is taken further, and we directly compare light curves produced at different wavelengths, we can see whether the variability is correlated between different regions of the AGN. If the variability is correlated, this implies that the source of the variability is connected across the structure. In addition, if there is a delay in the correlation, for example the X-ray flux changes and then the optical fluxes changes some time later, then it is likely that the variability started in the X-ray corona and was then reprocessed into the optical accretion disk (assuming the unified model is correct). The length of that lag tells us how long that light took to reprocess, and comparisons to the lags predicted by various AGN models could help further our understanding of their structure.

The differing timescales mentioned above mean that variability studies are very different depending on which waveband is being examined. Here we will discuss what is known about AGN variability at various wavelengths, along with any previous work on using variability to select AGN. This approach is particularly attractive because AGN are usually selected based on X-ray emission or their colours (see Section 1.1.2), but using variability allows us to find unusual AGN that would be missed by these methods.

1.2.1 X-ray Variability

Variability is easy to study in the X-ray regime as the timescale of variability (minutes–hours) is observable within observations of only a few hours. This ease of observing, along with readily available and well sampled long-term monitoring, has allowed us to develop a good understanding about the X-ray variability of AGN at low redshifts. In fact, the majority of our current understanding of variability comes from the long term monitoring of AGN in the X-rays.

X-ray variability is thought to originate from independent flaring events in the hot corona of relativistic electrons (e.g. Almaini et al., 2000). This is evidenced in the well documented inverse relationship between variability amplitude and luminosity (e.g. Lawrence & Papadakis, 1993), as small variations due to independent flares will have less of an impact on the overall luminosity of a highly luminous AGN.

A significant feature of AGN variability is its "red noise" power spectral density (PSD), this means that the variability has larger amplitudes over longer timescales (e.g. Lawrence et al., 1987). Detailed studies of the X-ray PSD of AGN (such as Uttley et al., 2002; Edelson & Nandra, 1999) have shown that there is a characteristic shape for X-ray AGN PSDs, which is a steep slope of ~ -2 on short timescales, that flattens to a slope of ~ -1 at a "break frequency". The break frequency is thought to be caused by a physical process occurring at a certain radius but there is no definitive view as to what that process is. This is because there are many processes that have similar timescales and there are a number of unknowns within accretion disk physics (such as the scale height) that make it difficult to constrain the cause. McHardy et al. (2006) showed that the break frequency decreases with increasing black hole mass, a characteristic that links AGN to stellar mass black holes in X-ray binary systems. This similarity suggests that the variability in both systems could be caused by the same underlying physics.

1.2.2 UV/Optical Variability

Until recently, studying the variability of large numbers of optical AGN was difficult, as fields were rarely monitored for extended periods, and if repeat measurements were taken data was irregular and patchy. Early optical variability studies, such as Peach (1969) and Lu (1977), focused on the light curves of single, nearby AGN. However, as data becomes more readily available, studying the optical variability of large samples of AGN is a growing research area. Large surveys like the Sloan Digital Sky Survey (SDSS) can be used to identify variable quasars, as demonstrated by Butler & Bloom (2011) and MacLeod et al. (2016) among others, and dedicated variability studies such as those by Sanchez et al. (2016) and Caplar et al. (2017) are providing insights into the optical variability of known AGN.

These studies have started to show that the UV/optical PSD does not follow the universal shape discussed in Section 1.2.1; instead the PSD slope at high frequencies is steeper and the break frequency is higher with no dependence on BH mass. One of the most interesting discoveries in this regime are the inter-band lags of $\sim$ 1 day, where the red wavebands lag the blue (e.g. Sergeev et al., 2005). These timescales seem to support the hypothesis that the variability originates in the X-ray before propagating out through the accretion disk (e.g. Cackett et al., 2007; Edelson et al., 2015). However the amplitudes of variations seen in some sources are too large to be attributed to reprocessing (e.g. Arévalo et al., 2009; Lawrence, 2018).

Other studies, such as McHardy et al. (2014), have correlated optical with X-ray light curves to determine where the variability comes from, and how it propagates through the AGN. On short timescales (days-weeks), optical variability is thought to be caused by reprocessing of the X-ray variability into the accretion disk, as optical variations have been seen to follow the X-ray variations on timescales that correlate with the light travel

time from the X-ray corona to the accretion disk. In addition, the lags have been shown to increase with wavelength (lag $\propto \lambda^{\sim\frac{4}{3}}$), as expected from accretion disk modelling. The reprocessing is thought to occur when the change in the X-ray corona illuminates the accretion disk, which causes its temperature (and therefore its luminosity) to change. On long timescales (months-years), optical variations do not generally follow the X-ray patterns (e.g. Arévalo et al., 2009; Uttley et al., 2003), and therefore this variability is thought to be caused by accretion variations in the disk, especially as long-term variability occurs on viscous timescales.

1.2.3 Near-infrared Variability

NIR variability is particularly interesting as it probes rest-frame red optical light at high redshifts, allowing comparisons to variability in the local universe. In addition, rest-frame NIR light has been shown to originate in both the accretion disk and the dusty torus (Lira et al., 2011; Landt et al., 2011). Previous NIR studies have generally either used observations of previously known AGN to confirm that AGN do vary in the NIR (e.g. Enya et al., 2002) or used ensemble variability to characterise the variations (e.g. Kouzuma & Yamaoka, 2011).

Some of the longest NIR AGN light curves studied to date are presented in Neugebauer et al. (1989) and Sánchez et al. (2017). Neugebauer et al. (1989) explored the NIR variability of individual AGN by using a number of different datasets to construct light curves spanning an average of 6 years, with some covering up to 20 years. Sánchez et al. (2017) examined the NIR light curves of individual AGN over approximately 5 years, using photometric data from the UltraVISTA survey (McCracken et al., 2012). In both cases, the AGN were selected in different wavebands: Neugebauer et al. (1989) used optical selection, while Sánchez et al. (2017) studied a sample of X-ray selected AGN.

The origins of rest-frame NIR variability are not yet understood, although the timescales of the variations (months-years) suggest that they arise from viscous processes or a large torus, as these timescales are too large for the variations to be attributed to simply the reprocessing of X-ray variations in an accretion disk. Studies of lags between NIR wavebands and optical or X-ray wavebands, such as those presented in Lira et al. (2011, 2015), show lags varying from a few days to a few months. These differences were attributed to differences in BH mass, and to whether a torus is thought to be present in the system. This shows that, while studies of individual AGN allow us to understand that particular source in great detail, the underlying physics of one system might not hold in a system with different properties. A systematic study of a large sample of NIR AGN light curves is needed to discover if there is a typical lag length, and what this could tell us about the AGN population as a whole.

Selection by NIR variability had not been attempted prior to the publication of Chapter 2 in Paper I. This is because a survey with a long baseline of observations, approximately 5 to 10 years, is required to detect the high amplitude variations. In addition to this, deep data is needed to allow the detection of faint, high redshift objects and studies of small amplitude variability, and a wide survey area is necessary in order to find rare types of AGN from just the variability data.

1.3 Thesis Structure

This thesis investigates selecting AGN through their long-term variability in the NIR, before going on to discuss the properties of these variable AGN.

- In Chapter 2, we describe the UKIDSS Ultra Deep Survey (UDS) data used in this thesis. This dataset included photometric and spectroscopic catalogues in

addition to stacked images. We describe the image processing that was applied to the stacked images to prepare them for variability analysis, and the measurement of accurate photometric uncertainties. Finally, we outline the selection method for finding AGN based on their long-term variability in the K-band. This work is published in Paper I.

- In Chapter 3, we discuss how the K-band variability selected AGN compare to AGN selected in the X-rays and MIR. This work is also published in Paper I.

- In Chapter 4, we extend the selection method described in Chapter 2 to also select variables in the J-band. We will complete a comparison to the X-ray selected AGN, and then compare the J-band selected variable AGN to the K-band selected variable AGN to determine if there are differences between the AGN selected in each band.

- In Chapter 5, we extend the data preparation steps discussed in Chapter 2 to produce light curves on monthly timescales. We then use the short timescale light curves to investigate correlations between the J- and K-band light curves, and to determine if there are any lags between them. This work was published in Paper II.

- In Chapter 6 we summarise our results, present the conclusions from this work, and discuss what future work on this topic could involve.

Throughout this thesis we adopt a ΛCDM cosmology with $H_0 = 70$ kms^{-1} Mpc^{-1}, $\Omega_\Lambda = 0.7$, $\Omega_m = 0.3$.

Chapter 2

Selecting AGN using Long-term K-band Variability

In this chapter we present the first attempt to select AGN using long-term near-infrared (NIR) variability. By analysing the K-band light curves of all the galaxies in the UKIDSS Ultra Deep Survey (UDS), the deepest NIR survey over $\sim$ 1 sq degree, we have isolated a sample of variable AGN candidates through a χ^2 analysis. We will discuss the UDS data as a whole (Section 2.2), as well as the specific image preparation steps required to produce light curves suitable for variability analysis (Section 2.2.1), before finishing with the details of the selection technique in Section 2.3.

2.1 Introduction

There are a variety of methods that can be used to select Active Galactic Nuclei (AGN) from pre-existing catalogues, using both photometric (e.g. Stern et al., 2005; Lacy et al., 2004, 2007) and spectroscopic (e.g. Feltre et al., 2016) criteria, and each of them has both strengths and weaknesses. For example, some methods are geared towards low

redshift samples, and can become highly contaminated at high redshifts (Donley et al., 2008). Padovani et al. (2017) gives an overview of identification techniques across the electromagnetic spectrum, and their selection effects. Selecting AGN through X-ray emission is generally accepted to be the most complete method. However, deep X-ray surveys will miss heavily obscured AGN, and are expensive as they require long exposure times on premium telescopes, such as Chandra.

It is well established that the light from AGN changes over time (e.g. Angione, 1973). This characteristic can be used to select AGN, and to study the physics of the system on scales that are difficult to resolve with standard observational techniques. Selection by variability has been previously undertaken in the optical/UV (e.g. Pouliasis et al., 2019; Sánchez-Sáez et al., 2019) and X-ray (e.g. Young et al., 2012) regimes. Section 1.2 provides more details of previous variability studies across the electromagnetic spectrum.

As discussed in Section 1.2.3, selection by NIR variability has not previously been attempted due to the long-term nature of the variations. The majority of variations in the NIR light curves of AGN are only expected to be observable from year to year (e.g. Neugebauer et al., 1989). Although there is evidence of small amplitude variations on shorter timescales (e.g. Sánchez et al., 2017), AGN variability typically has a red noise power spectrum so the largest amplitude variations are seen over long timescales (e.g. Lawrence et al., 1987). As such, selection through NIR variability on long timescales ought to provide a relatively clean sample of AGN, and in principle ought to be less sensitive to dust obscuration compared to optical/UV techniques; the main contaminants are expected to be variable stars and supernovae.

The United Kingdom Infrared Telescope (UKIRT) Infrared Deep Sky Survey (UKIDSS) Ultra Deep Survey (UDS) is the perfect data set for a study of this kind. The long baseline probes the timescales where previous works have found interesting

variability, and, as the deepest NIR survey over such a wide area, it is deep enough to find faint AGN, while still covering a large enough area to find rare objects amongst the AGN population.

This chapter focuses on selecting AGN using only their variability in the NIR, and the selection method is presented in Section 2.3. The unique nature of the UDS, combined with removing any prejudice introduced by prior selection techniques, means that this study can probe AGN in ordinary host galaxies as well as bright quasars.

2.2 Data

The UDS provides a unique data set for studying NIR variability of AGN. In addition to being the deepest NIR survey over 1 deg^2, with a 5σ detection limits of $J = 25.6$, $H = 25.2$ and $K = 25.3$ (AB), the UDS has an unprecedented 8 year baseline for time domain studies with data taken between September 2005 and November 2012. The field is also well studied in a wide range of wavebands, including X-ray imaging of the whole field to a depth of $\sim 10^{-15}$ erg cm^{-2} s^{-1} with XMM (Ueda et al., 2008), deep Chandra imaging of the centre of the field ($F_{lim} \sim 10^{-16}$ erg cm^{-2} s^{-1} Kocevski et al., 2018), and imaging in all four bands of the Spitzer Infrared Array Camera (IRAC, Fazio et al., 2004; Dunlop et al., 2007).

The photometric redshifts were determined using the deep 12-band photometry available in the UDS field ($U, B, V, R, i', z', Y, J, H, K, 3.6, 4.5$), based on the method outlined in Simpson et al. (2013). A wide range of galaxy templates were used, using simple stellar populations from Bruzual & Charlot (2003), with fitting completed using the EAZY software (Brammer et al., 2008). The resulting photometric redshifts were then used to derive other galaxy properties, such as luminosities and stellar masses. Further details will be provided in Almaini et al. (in prep) and Hartley et al. (in prep).

The near-infrared imaging in J, H, K was obtained using the Wide Field Camera (WFCAM; Casali et al., 2007) at UKIRT. A single WFCAM observation of the UDS comprises 10s exposures with a 3 x 3 micro-step, in order to increase the pixel resolution of the images, and a 3 x 3 dither, which offsets the effects of bad pixels and flat-fielding complications. This adds up to a total exposure time of 810s per observation. As WFCAM consists of four 13.7 x 13.7 arcmin detectors with 12.9 arcmin between them, a total of at least 4 observations offset by $\sim$ 13 arcmin is required to cover the whole field. The total exposure times in J, H and K are 318.5, 203.5, and 476.6 hours respectively. Further details on the UDS observing strategy can be found in Lawrence et al. (2007) and Almaini et al. (in prep), and further details on how light curves were extracted from these images can be found in Section 2.2.1.

In addition to deep photometric data, there has been extensive spectroscopic follow-up of the UDS field. The main follow-up programme was the UDSz (ESO large programme 180.A-0776), which used the VIMOS and FORS2 instruments on the ESO VLT to obtain spectra for $>$ 3500 galaxies (see Bradshaw et al., 2013; McLure et al., 2013). Furthermore, the field was covered by the VANDELS spectroscopic survey (ESO programme 194.A-2003, McLure et al., 2018; Pentericci et al., 2018), providing $\sim$ 780 VIMOS spectra, and a follow up of post-starburst galaxies using VIMOS has also been completed, providing $\sim$ 100 additional spectra (Maltby et al., 2016). A further $\sim$ 4000 spectroscopic redshifts are provided from archival data, details of which can be found in Simpson et al. (2012) and references therein.

2.2.1 Light Curve Preparation

The images used in this analysis were stacks of all acceptable K-band observations taken during one semester of observing. The stacks were created from an adapted version

of the SWARP software (Bertin et al., 2002), and only observations that met strict quality controls were included. These controls included restrictions on values of seeing, ellipticity, zero-point and noise, and reduced the exposure times quoted in Section 2.2 by approximately 10%. The quality controls, and the SWARP parameter files, were carefully put together by the UDS team, see Almaini et al. (in prep) for more details. We chose to complete this initial study on semester stacks as using the stacked semester images allows us to probe faint, high redshift objects, and preliminary tests revealed that the majority of the variability could be seen on those timescales. This is expected as AGN variability follows a red noise pattern where the largest amplitude variability is seen on longer timescales (e.g. Lawrence et al., 1987). In addition, probing shorter timescales would considerably increase the amount of contamination by supernova and other variables. The K-band was chosen for this initial selection as the data was taken in the best seeing, it has the longest exposure time, and it is the deepest band for the selection of typical high-redshift galaxies. In Chapters 4 and 5, we extend this selection technique to the J-band data.

Before the photometry could be extracted from each stack and a light curve constructed, the stacks had to be processed to reduce potentially contaminating sources of variability. The steps involved in this data preparation are detailed below and involve cleaning the image, homogenising the seeing across the stacks, extracting the photometry, and finally determining accurate photometric uncertainties.

2.2.1.1 Cleaning

The first step in the data preparation was to clean the images. The cleaning aims to smooth the background, and remove defects such as remnants (when observing a bright star in the previous pointing has left a dark spot on the current observation) and striping in the WFCAM image background produced by the detector electronics. The code,

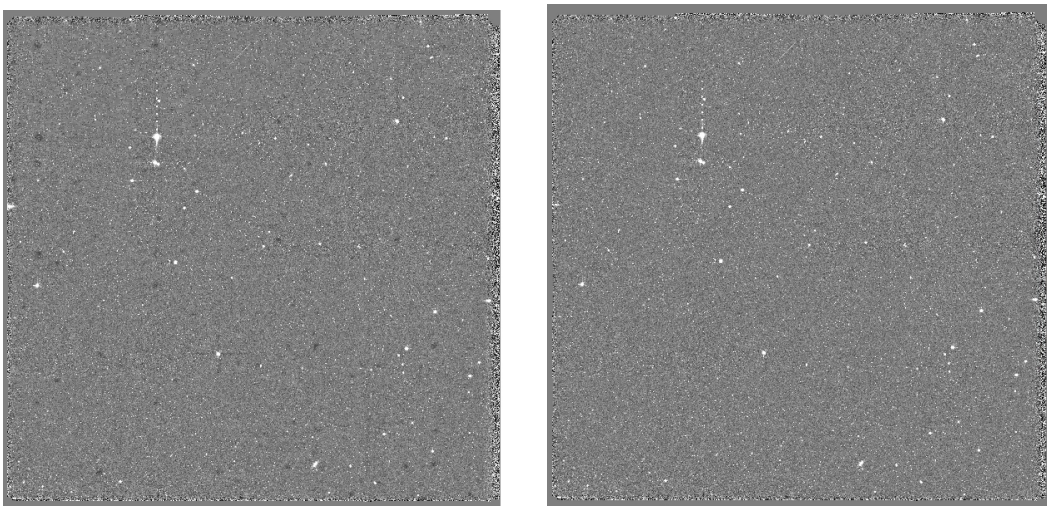

(a) Image stack of the 08B semester before cleaning.

(b) Image stack of the 08B semester after cleaning.

Figure 2.1: Demonstration of the improvement from cleaning the image stacks.

developed by William Hartley, involves using the segmentation map outputted from Source Extractor (SExtractor, Bertin & Arnouts, 1996) to identify regions of the field where there are no sources, then cleans this area using a cross-shaped median filter. This shape was chosen as it efficiently removes the striping seen in these deep NIR images. Figure 2.1 demonstrates the improvement from cleaning the image stacks.

2.2.1.2 Convolution

In order to ensure that the variations seen in the light curves of objects are truly those of the observed object, any other sources of variation must be taken into account. The main source of variations between semester stacks is changes in the point spread function (PSF). In order to minimise this effect, each stack was convolved with a Gaussian kernel to match the PSFs to the semester with the poorest PSF, which was the 2010B stack.

The PSFs were constructed by creating a 59 px x 59 px image of the median star based on a sample of $\sim$ 2000 stars in the magnitude range $15 < K_{2arcsec} < 19$. These

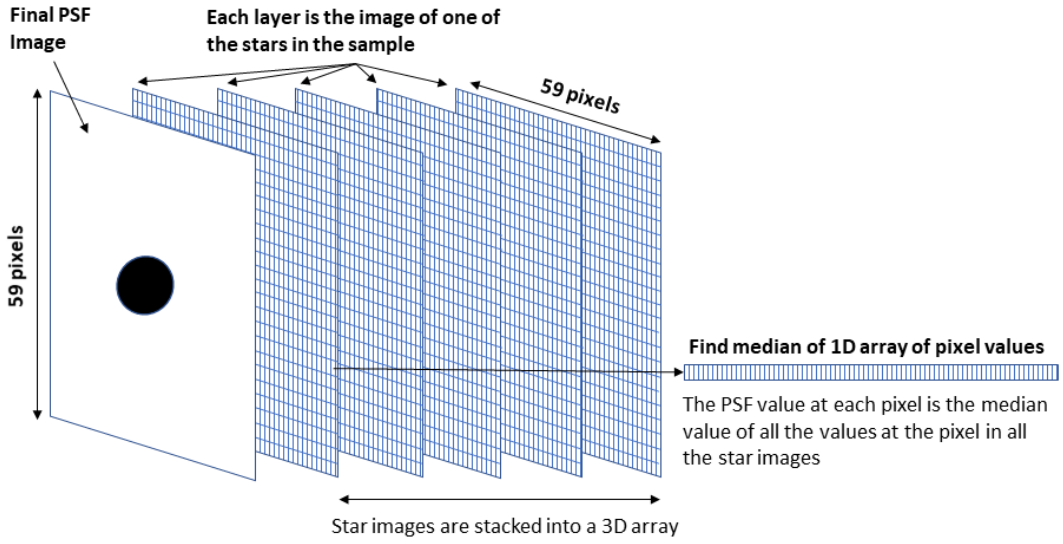

Figure 2.2: A schematic view of the manner in which PSF images were constructed

criteria were chosen to give a clean sample of unsaturated, point-like stars. The median image was created by finding the median value for each pixel across all of the stars, after the stars had been normalised. This process is visualised in Figure 2.2.

Once the PSFs had been constructed for each stack, the stack with the worst seeing was identified as the one with the largest mean FWHM, as determined from SExtractor. The value of σ for the Gaussian kernel then needs to be calculated. Originally, the σ of each PSF was determined and then an intial estimate of σ_{kernel} was constructed using

$$\sigma_{kernel} = \sqrt{\sigma_{aim}^2 - \sigma_{PSF}^2} \tag{2.1}$$

where σ_{aim} is the σ of the semester with the widest FWHM and σ_{PSF} is the σ of the semester whose PSF is being matched.

It was found that using this σ_{kernel} did not match the PSFs of the convolved images. This was likely because the PSFs are not perfectly Gaussian. Therefore, an extra factor was required to make the optimum convolution kernel. This factor turns Equation 2.1

into

$$\sigma_{kernel} = \sqrt{\sigma_{aim}^2 - \sigma_{PSF}^2} + extra \tag{2.2}$$

The value of $extra$ is individual to each stack and was determined by running a trial convolution on the PSF image. For each possible value of $extra$, a convolution kernel with the related σ_{kernel} was created and convolved with the PSF image. A radial profile of this was then determined, and compared to the radial profile of the aim PSF image. The value of $extra$ that produced a convolved PSF with the least difference between radial profiles was chosen. The convolution was then run on the full stacks, and the new stacks' PSFs were compared to ensure that the convolution had worked as expected.

The impact of this convolution is best visualised by examining the differences between radial profiles of the PSFs before and after convolution. Figure 2.3 shows that before the K-band semester stack convolution there are large differences between the radial profiles, especially around the central peak, but these differences are largely eliminated by the convolution. The improvement is also quite clear when you compare the FWHM values of the PSFs before and after the convolution.

2.2.1.3 Image Extraction

As the UDS field is only visible in the second semester of a year, there are a total of 8 epochs across the whole survey. Unfortunately, not enough observations were taken in the 2006B semester (Figure 2.5), and therefore the image is dominated by noise. Accordingly, 2006B was not included, and the final analysis was undertaken using 7 epochs spanning 2005 to 2012. Photometry was extracted from these stacks by placing 2 arcsec apertures at the position of every object identified in the final DR11 image of the UDS using the SExtractor software. A 2 arcsec aperture was chosen as it is optimises the trade off between the aperture being large enough to minimise the effect of changing

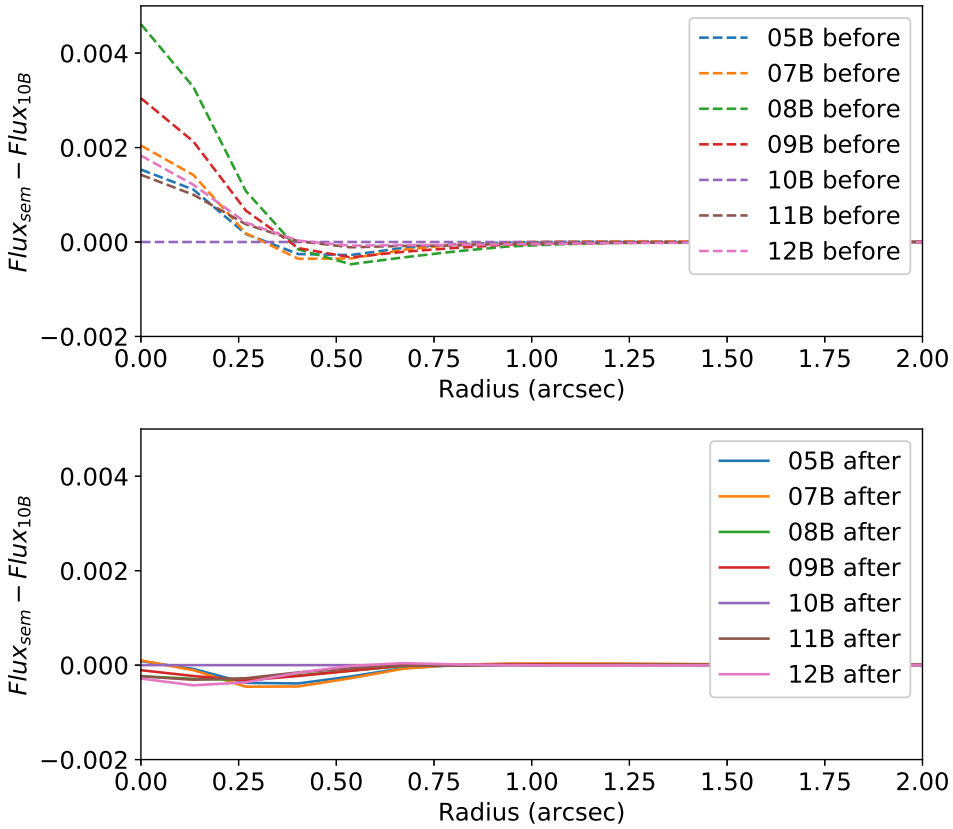

Figure 2.3: The difference between the radial profiles of the PSFs in each semester relative to 10B, before (top) and after (bottom) convolution. The PSFs were created using $\sim$ 2000 stars in the magnitude range $15 < K_{vega} < 19$. The differences seen in the top panel are drastically reduced by the convolution.

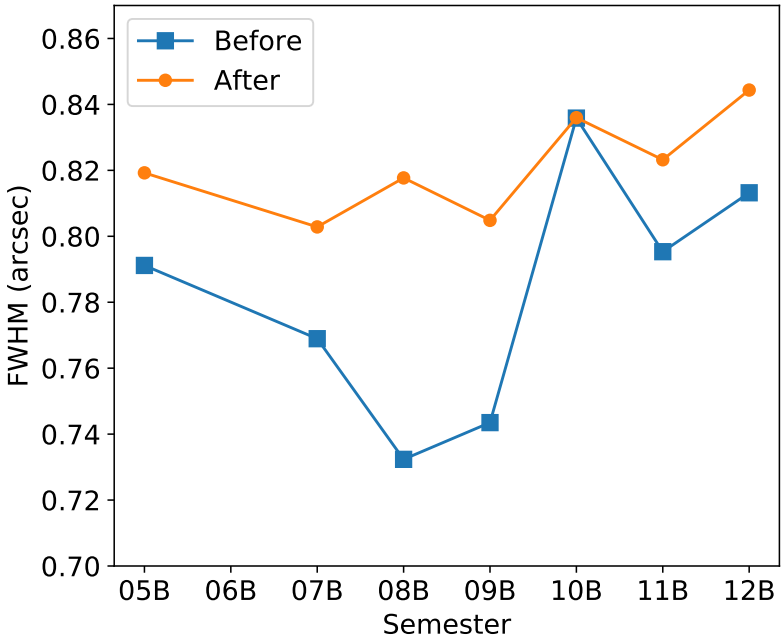

Figure 2.4: The difference between the full width half maximum values of the semester PSFs before and after the convolution.

seeing on the light curves, and small enough to minimise dilution of the variability by the host galaxy.

The zeropoints of the UDS images were calibrated from 2MASS stars, and were verified against other deep surveys in the field (see Almaini et al., in prep, for details). If there are residual variations in zeropoint between the semester stacks, these would be taken into account in the determination of photometric uncertainties described in Section 2.2.1.4.

2.2.1.4 Photometric Uncertainties

As the photometric uncertainties from SExtractor are typically underestimated (Molino et al., 2014; Sonnett et al., 2013), we instead use uncertainties that were self-calibrated from the data. The method used was tailored to take into account any remaining

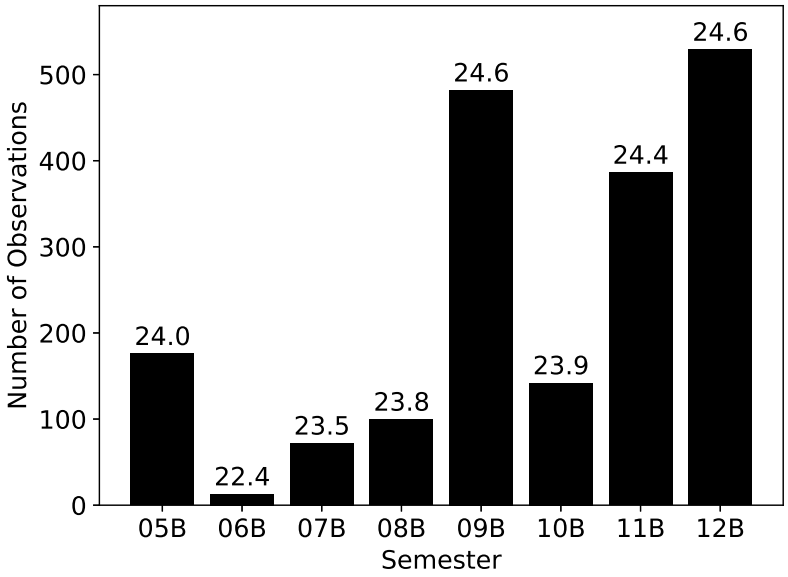

Figure 2.5: Bar chart to show the number of 810s observations included in each semester stack. The numbers at the top of the bars indicate the K-band 5σ detection limits in AB magnitudes for each of the semester stacks. The 06B semester did not have enough observations to be included in the analysis.

variations due to noise or systematic effects. In order to ensure these effects were incorporated into the uncertainties, we used the spread of flux values in the non-varying sources to provide a direct estimate of the uncertainty on the flux. The varying sources were excluded from the analysis by modelling the uncertainties as the characteristic variance with flux, and running a preliminary χ^2 analysis to remove those with significant variability. This process was then iterated to ensure the model wasn't skewed by the varying sources. The light curves of non-varying sources were then normalised and split into bins of flux (determined from the overall stack, with widths equivalent to $\Delta mag = 0.1$), epoch and quadrant. Within each bin, the standard deviation of the normalised flux values then provided the calibrated photometric uncertainty on any object in that bin. This process and the improvement from SExtractor errors is demonstrated in Figure 2.6. Examples of the resulting light curves with these uncertainties are shown in Figures 2.7 and 2.8.

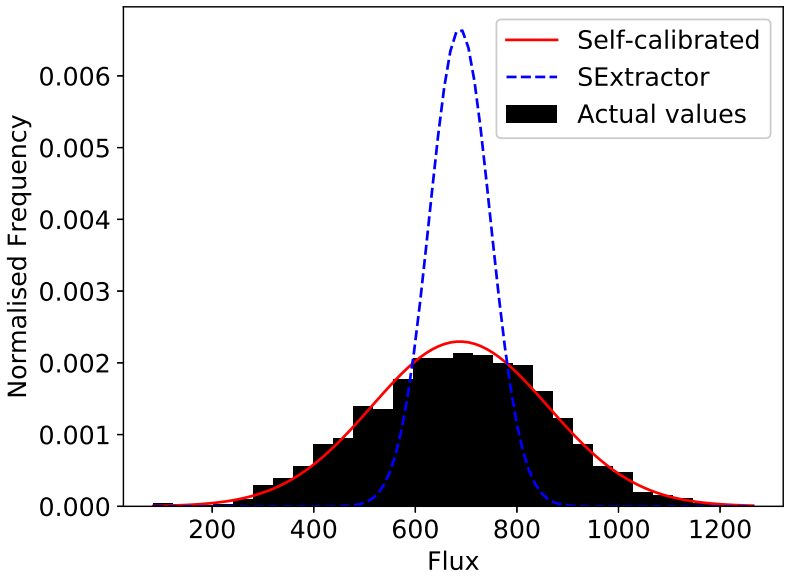

Figure 2.6: The distribution of flux values within a single quadrant, epoch and flux bin. The red solid line indicates the Gaussian fit to the data when the self-calibrated σ_F value is used. The blue dashed line shows the Gaussian fit using the median σ_F value outputted from SExtractor in that bin.

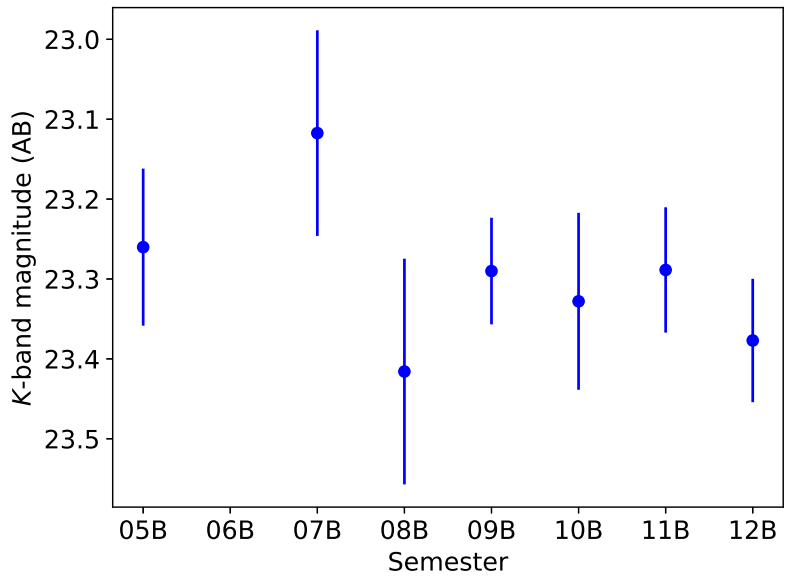

Figure 2.7: An example of a non-variable light curve with $\chi^2 = 4.26$.

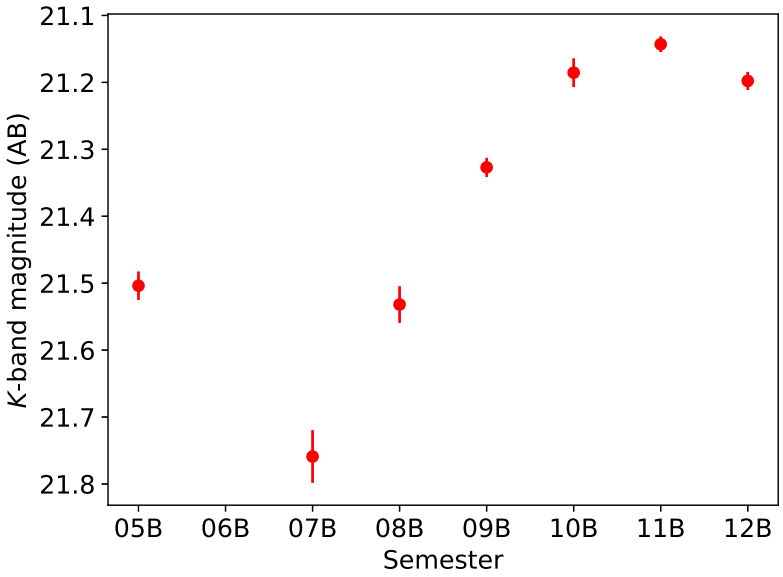

Figure 2.8: An example of a variable light curve with $\chi^2 = 710.03$.

2.3 Selection Method

Before the selection was completed the catalogue was masked to exclude regions that are too close to bright stars or affected by image artefacts, and any objects that had negative flux values in any semester were removed from the catalogue. We acknowledge that some of the most extreme variables may be removed in this final step, but for our purposes we require a visible source in every epoch in order to ensure that our photometric redshifts are as reliable as possible (see Section 3.1). We also required that each object had optimal coverage in all 12 photometric bands. Known Galactic stars were also excluded from the analysis as they are the only other objects expected to vary on these timescales. These stars were identified using a combination of SED fitting and image profiling that robustly separates stars and galaxies based on both colours and morphology (for more details see Simpson et al., 2013, and Almaini et al. in prep); a total of 5592 objects were excluded. Supernova are unlikely to be a significant source of contamination on yearly timescales as all but the most extreme cases will average

out within the semester stack. The original catalogue contains 296,036 sources; this is reduced to 152,682 sources by these criteria.

The variable source selection method involves constructing a light curve for each object from the 7 semester stacks, and running a χ^2 analysis. For this work we define

$$\chi^2 = \sum_i \frac{(F_i - \bar{F})^2}{\sigma_i^2} \tag{2.3}$$

where F_i is the flux of an object in an epoch, $\bar{F}$ is the average flux of that object across all epochs, and σ_i is the uncertainty on F_i. The χ^2 statistic provides a simple test of the null hypothesis that a source is non-variable. The complete selection is demonstrated in Figure 2.9, which shows the distribution of χ^2 values as a function of flux. A threshold of $\chi^2 > 30$ was used to define which sources are considered variable; this value was chosen as it minimises the expected number of false positives while maximising the number of variables found. From a χ^2 distribution with 6 degrees of freedom within each flux bin, we expect less than one false positive above this threshold. Over the whole data set, a total of 6 false positives would be expected. When applied to the reduced catalogue described above, the method found a total of 393 variable sources, representing a density of $\sim 550/\mathrm{deg}^2$. The spatial distribution of the variables was checked to ensure they were randomly distributed.

Although this sample does not include any objects identified as stars in the UDS catalogue, we completed independent colour and morphology tests to ensure there was minimal stellar contamination. These checks involved quantifying whether the light profiles of the objects appeared 'stellar', and using colour-colour plots (such as those used in Sánchez-Sáez et al., 2019; Lane et al., 2007) to examine whether the variables had colours consistent with stars. All of the 393 variables had resolved (galaxy-like) morphologies and optical/IR colours that are not consistent with the stellar locus.

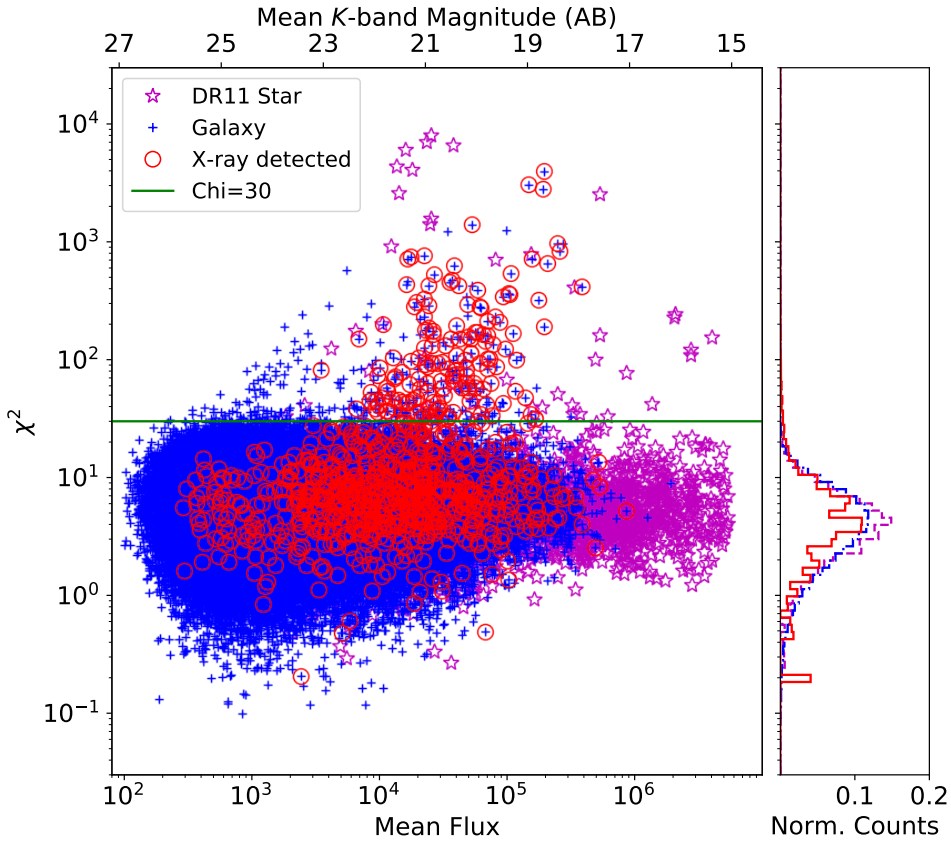

Figure 2.9: χ^2 against mean K band flux for all the objects in the UDS field that are observed in all 7 semesters, the green line indicates the selection threshold.

2.4 Summary

In this chapter, we have presented a new method of AGN selection using only the K-band light curves of objects in the UDS. Initially, the data had to be prepped to ensure that there were minimal systematic variations in the data, this included normalising the PSFs across all epochs and ensuring accurate photometric uncertainties. The selection method then involved applying a χ^2 analysis to the light curves of non-stellar objects with detections in all 7 epochs. A selection threshold of $\chi^2 = 30$ was chosen in order to minimise false detections while maximising the number of variables identified. This gave a sample of 393 variable AGN across the UDS field.

In Chapter 3 we will investigate how this sample of variable AGN compares to samples of AGN selected using X-ray and mid-infrared selection techniques. In Chapter 4 we will extend this selection to also select based on the J-band light curves, and examine what difference this makes to the selected AGN. Finally, in Chapter 5 we will use the image preparation steps outlined in Section 2.2.1 to create light curves using stacks on monthly timescales, and use these to investigate time delays between the J- and K-band light curves on shorter timescales.

Chapter 3

Investigating AGN Selected Using Long-term K-band Variability

In this chapter, we examine the population of variable Active Galactic Nuclei (AGN) selected in Chapter 2. We compare the variable AGN to those selected using deep X-ray AGN imaging and mid-infrared colours to see if variability selected AGN have any unique properties. In addition, we will discuss potential sources of contamination in the sample and how these have been accounted for. This work was published in Paper I.

3.1 Comparison to other AGN populations

3.1.1 X-ray AGN

If a high redshift source is bright in X-rays, there as a very high likelihood that it is an AGN. As such, deep X-ray imaging is a clean and relatively complete method of finding AGN in deep sky surveys (Padovani et al., 2017). The main contaminants in X-ray imaging are stars, but in the UDS the star/galaxy separation is generally reliable,

	Chandra Region (Chandra)	Full Field (XMM and Chandra)
X-ray Selected AGN (A)	593	1247
Variability Selected AGN (B)	181	393
% of A that are also B	12%	13%
% of B that are also A	41%	42%

Table 3.1: Summary of the X-ray and NIR-Variable AGN samples. Numbers in each set are shown for the central region imaged with Chandra and the full field imaged with both XMM and Chandra.

and therefore stars are easily identified and removed.

The X-ray AGN catalogue was constructed from the deep Chandra imaging covering the central region of the UDS field (Kozłowski et al., 2016). Within this region, there are 593 X-ray AGN with associated K-band detections in the DR11 catalogue; sources were matched between X-ray and NIR data to within 1 arcsec. 74 (41%) of the 181 variable sources within the Chandra field are in the X-ray AGN sample, which is convincing evidence that the variability method does detect AGN. This proportion remains relatively constant if the analysis is extended to include the shallower XMM imaging of the whole field (167, 42%, of 393 variables), indicating the non-detections are not biased by the flux limits of the surveys (see Section 3.2.1). The relative numbers in each sample are outlined in Table 3.1.

Figure 3.1 shows the distribution of stellar masses with redshift for all galaxies in the UDS. When the X-ray and variable AGN populations within the Chandra region are highlighted, it is clear that the variability analysis finds AGN across the parameter space, whereas the deep Chandra imaging only probes the high mass end. A KS test of the stellar mass distributions confirms that the variable and X-ray populations have significantly different distributions in stellar mass, with a p-value of 7.8×10^{-13}.

In addition, examining the X-ray-to-optical luminosity ratios of both the variable

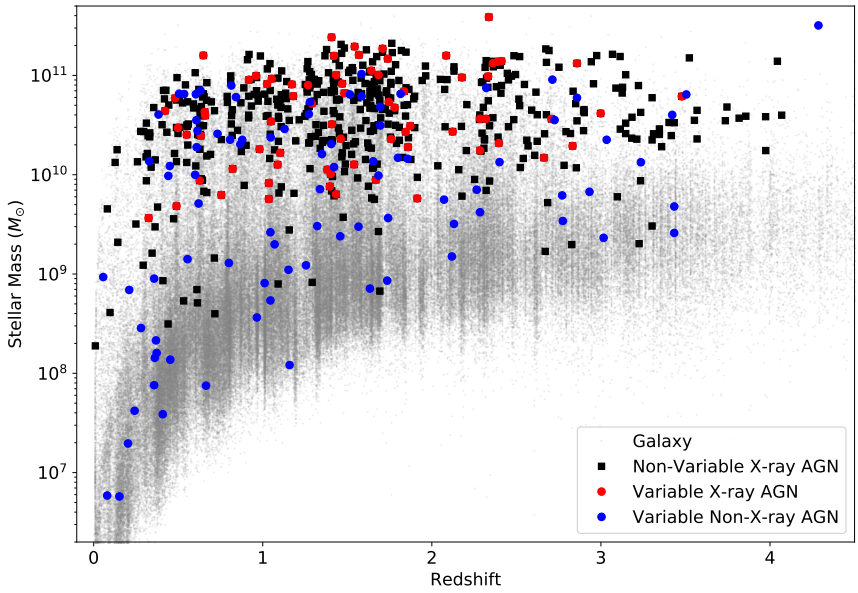

Figure 3.1: Stellar mass distribution with redshift showing where the X-ray and variable AGN populations sit within the parameter space, restricted to only the sources within the Chandra region. Variability selected AGN are found to occupy a wider range in stellar mass.

and X-ray AGN populations (Figure 3.2) shows that the variability method selects AGN that have lower luminosities (also shown in Figure 3.3), and there is evidence that these variable AGN are systematically X-ray quiet as they have higher α_{OX} values.

This evidence suggests that the AGN selection method presented here finds AGN that are systematically more X-ray quiet than the Chandra AGN, and therefore probes a low mass population that the deep Chandra data cannot detect. This results in a set of AGN that would be missed by the most common AGN selection technique in deep surveys.

3.1.2 IRAC AGN

The "Stern Wedge" (Stern et al., 2005) is another frequently used method for identifying AGN, in this case through their IRAC colours. It uses the four IRAC bands to define a

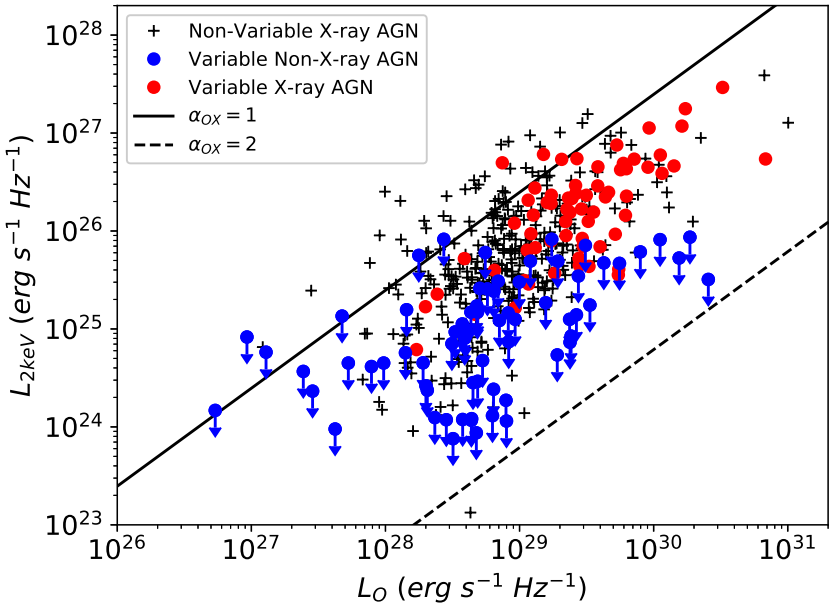

Figure 3.2: Monochromatic X-ray luminosity at 2 keV against monochromatic optical luminosity at 2500 Å. The solid line indicates where $\alpha_{OX} = 1$, and the dashed line shows $\alpha_{OX} = 2$, where α_{OX} is the point-to-point spectral slope between 2 keV and 2500 Å in the restframe. The X-ray luminosities for the non-X-ray detected variable sources are upper limits, as indicated by the blue arrows.

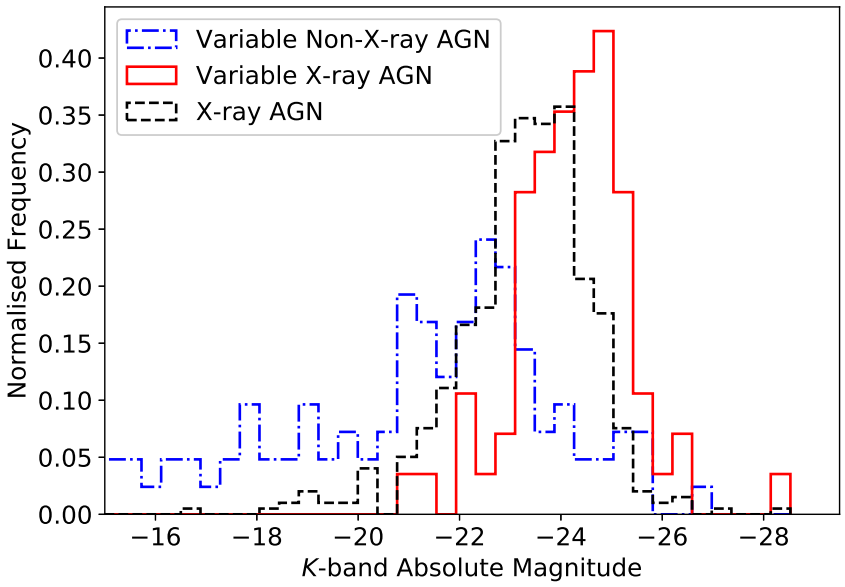

Figure 3.3: Normalised histogram of K-band absolute magnitudes showing that the 3 populations of AGN sample different luminosity ranges.

wedge within which sources are deemed AGN; the selection boundaries are shown by the green dashed lines in Figure 3.4. While there is significant contamination in this sample from star-forming galaxies at high and low redshifts (for more details, see Donley et al., 2008), it is nonetheless useful to examine any overlap between the techniques. In total, there are 6417 sources in the UDS that meet the Stern AGN criteria: 188 of theses are also variable AGN.

When comparing the Stern and variability selected samples, it should be noted that a source must have detections in all four IRAC bands to be selected by the Stern method. Only 249 of the variable AGN meet that criterion, and of these 76% are also Stern AGN.

Figure 3.5 shows the same plot as Figure 3.1 with the Stern and variable AGN that have full IRAC detections highlighted. While the difference between those that are in both samples and those that are only seen in the variable sample is not as strong here, this is only because the low mass variable AGN that were seen in Figure 3.1 are not found in the IRAC catalogue. Therefore, the variability study probes a low mass region that is also missed by the Stern selection method.

3.1.3 Catalogue Comparison

The above comparisons have shown that the variability analysis seems to find AGN across a wider range in stellar mass than either X-ray or IRAC selection methods. There are a total of 185 variables in the full sample that are not detected by either of the other selection methods, and these typically have lower stellar masses and luminosities.

While the Stern method selects the most AGN, it is also the most contaminated sample. This contamination makes comparisons between the variable and Stern AGN samples redundant. Therefore, when comparing the physical properties of the different AGN samples in Section 3.2, we focus on the comparison with X-ray selected AGN.

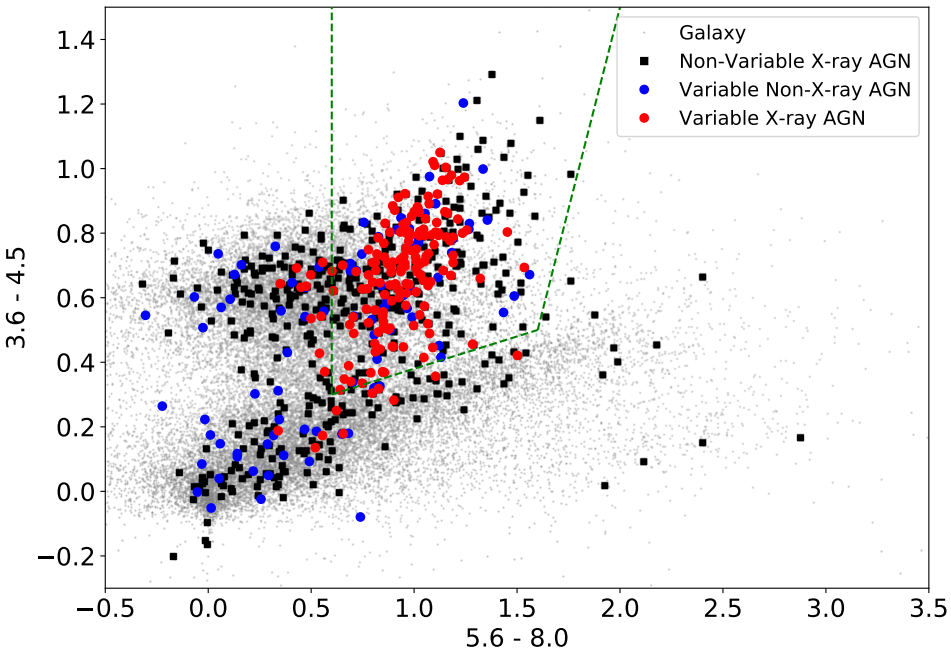

Figure 3.4: Stern AGN selection plot of mid-infrared colours. AGN are known to sit within the wedge indicated.

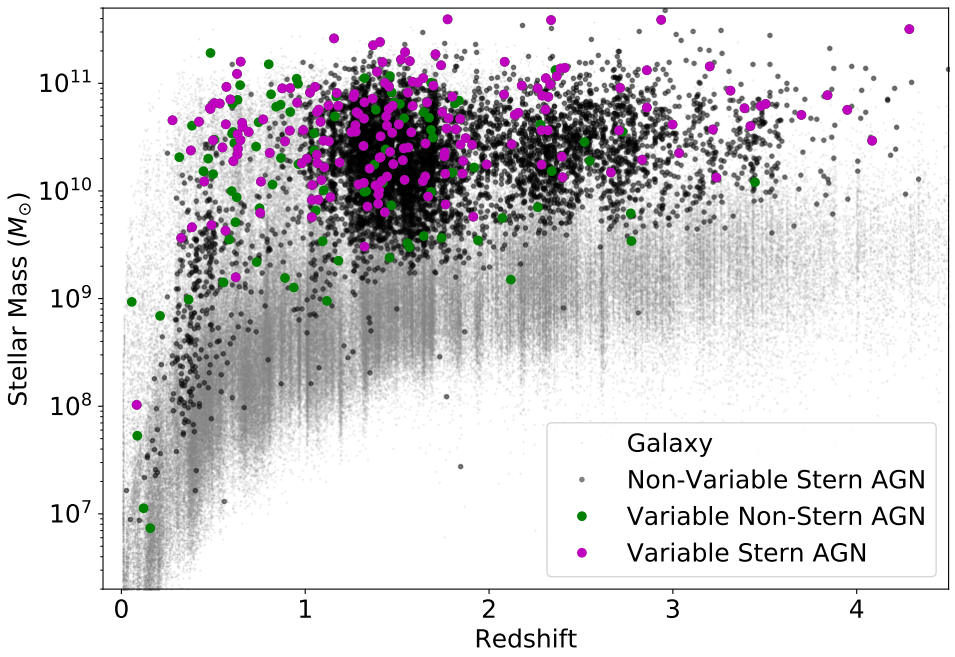

Figure 3.5: Stellar mass distribution with redshift showing where the Stern and variable AGN populations sit within the parameter space. Only those variables with detections in all 4 IRAC bands are shown here.

3.2 Characterising AGN

3.2.1 X-ray Detected and Non-X-ray Detected Variable Sources

As mentioned in Section 3.1.1, the variable non-X-ray detected sources appear to be a different class of AGN from the variable X-ray detected sources. When plotted on a rest-frame UVJ colour-colour diagram (Figure 3.6), which is commonly used to differentiate quiescent and star-forming galaxies, the variable X-ray detected sources are generally bluer than ordinary galaxies in U-V, consistent with some AGN contribution in UV light, while the variable non-X-ray detected sources do not show this excess UV light in general, which might be due to a more obscured central AGN or a low-luminosity AGN (LLAGN).

Looking into the IRAC colours of the populations beyond simply using them for selection can also provide insight into these sources. The variable non-X-ray detected sources are once again seen scattered through the galaxy locus in both Figures 3.4 and 3.7, while the variable X-ray detected sources are slightly offset. This adds further weight to the idea that these populations are dominated by different types of AGN.

While we have spectroscopic redshifts for a significant fraction of the variable sources (71 in total within the Chandra region, 56 X-ray detected and 15 non-X-ray detected), we only have access to 20 spectra for the variable sources; 12 of these are for the X-ray detected sources and 8 for the non-X-ray detected sources. The sources for these redshifts and spectra were discussed in Section 2.2.

From examining the limited spectra available, we find that the spectra of variable non-X-ray detected sources show features consistent with a different AGN population to those of the variable X-ray detected sources. The variable X-ray detected sources are generally found to have broad line AGN spectra (e.g. Figure 3.8), while the spectra

of variable non-X-ray sources are typically dominated by the light of the host galaxy (e.g. top of Figure 3.9). Among the variable non-X-ray AGN we also identify a rare Broad Absorption Line (BAL) quasar (Weymann et al., 1981), showing the characteristic blue-shifted absorption in the CIV line (bottom of Figure 3.9), which suggests that NIR variability could be effective at finding rare and interesting types of AGN. The light curves for those objects whose spectra are shown in Figures 3.8 and 3.9 are shown in Figures 3.10 and 3.11 respectively. It was not possible to determine any physical characteristics of the AGN simply from examining the light curves, but, from comparing these to the month timescale light curves that are presented in Chapter 5, we can say that the light curves follow the characteristic red noise pattern of AGN light curves (see Section 1.2.1).

The hypothesis that the variable non-X-ray detected sources are typically LLAGN is given further weight by Figures 3.2 and 3.3. These figures highlight that the variables not detected in X-rays have lower luminosities on average in the X-ray, optical and NIR regimes than the variables that are detected in X-rays. In addition, we know from Figure 3.2 that variable non-X-ray AGN are more X-ray quiet than the variable X-ray detected AGN population. This leads to the conclusion that long-term NIR variability studies can highlight populations of LLAGN that are missed by other selection techniques.

3.2.2 NIR-variable and non-variable sources detected in X-rays

While about half of the variable sources are detected in X-rays, there are a large number of X-ray sources in the UDS that do not have significant variability in the NIR. Figure 2.9 shows that the majority of the X-ray sources ($\sim$ 86%) sit within the main distribution of non-varying sources. This raises the question: what makes the X-ray sources that do

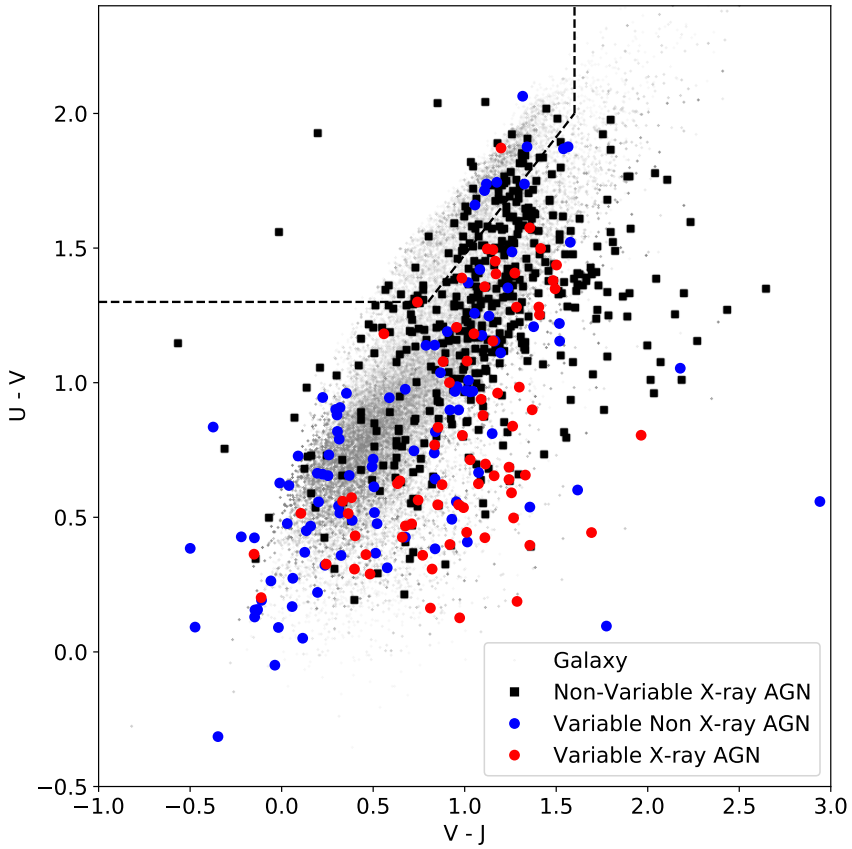

Figure 3.6: A rest-frame UVJ colour-colour diagram, used to differentiate quiescent and star-forming galaxies. Quiescent galaxies are found in the top left of the diagram, as defined by the dashed line, while star-forming galaxies and quasars are found in the remaining regions. The plot demonstrates that the majority of the variable AGN have rest-frame optical colours consistent with star-forming galaxy hosts.

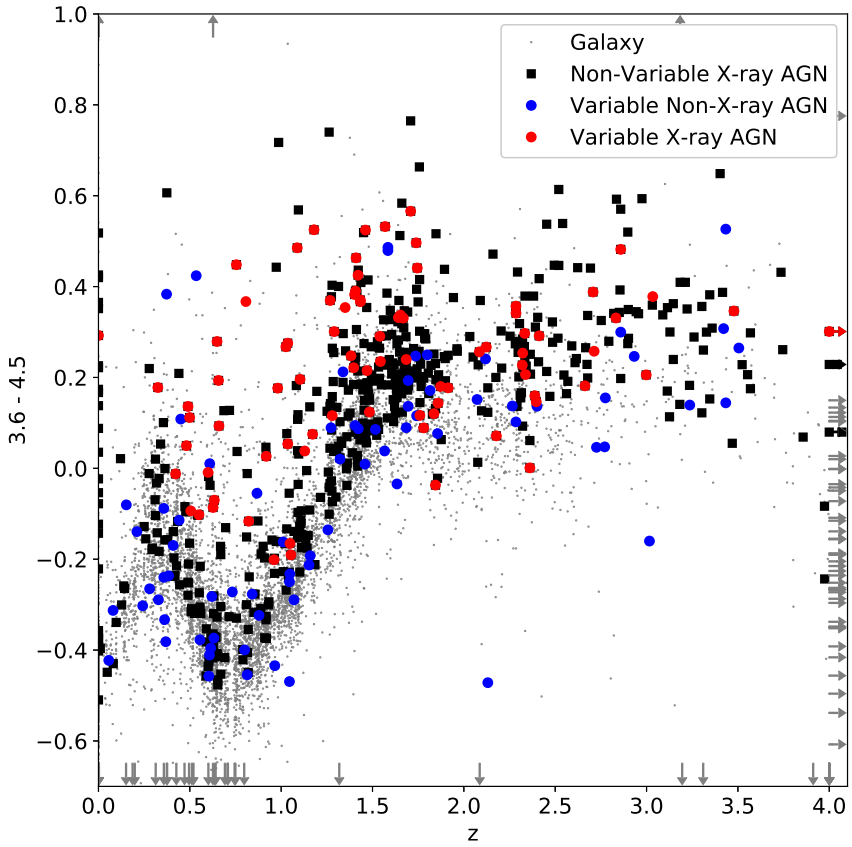

Figure 3.7: 3.6 - 4.5 micron colour as a function of redshift. AGN usually sit above the galaxy locus in this space.

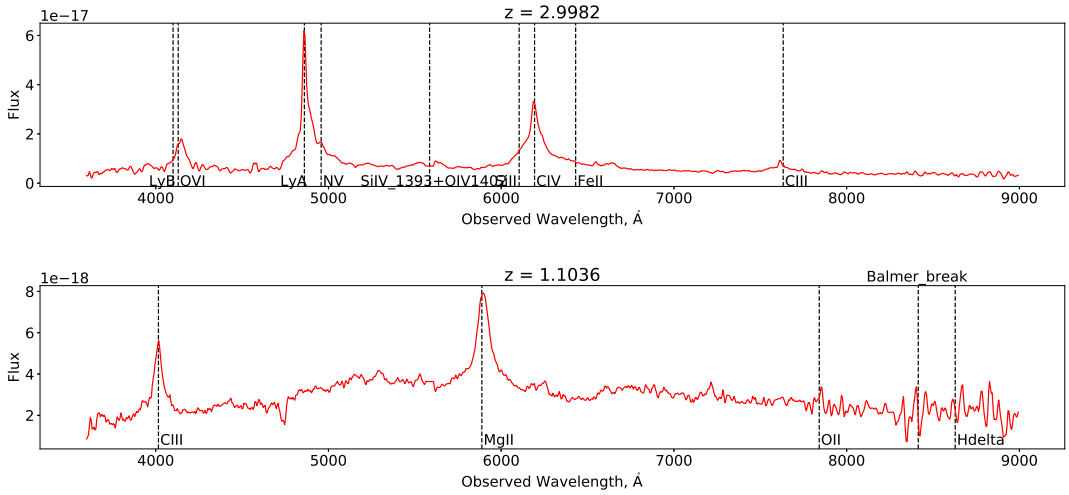

Figure 3.8: Spectra of two X-ray detected variable AGN. Both spectra are VIMOS spectra from UDSz.

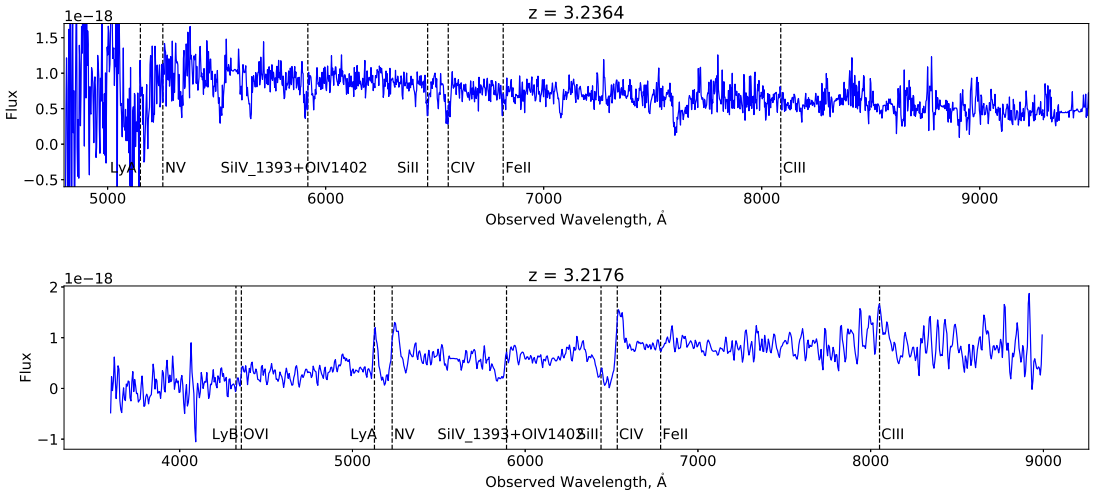

Figure 3.9: Spectra of two variable AGN that are not detected in X-rays. The top figure shows a VLT VIMOS spectrum from VANDELS of a normal $z \sim 3$ star-forming galaxy, while the bottom figure shows a VIMOS spectrum from UDSz that reveals a candidate BAL quasar.

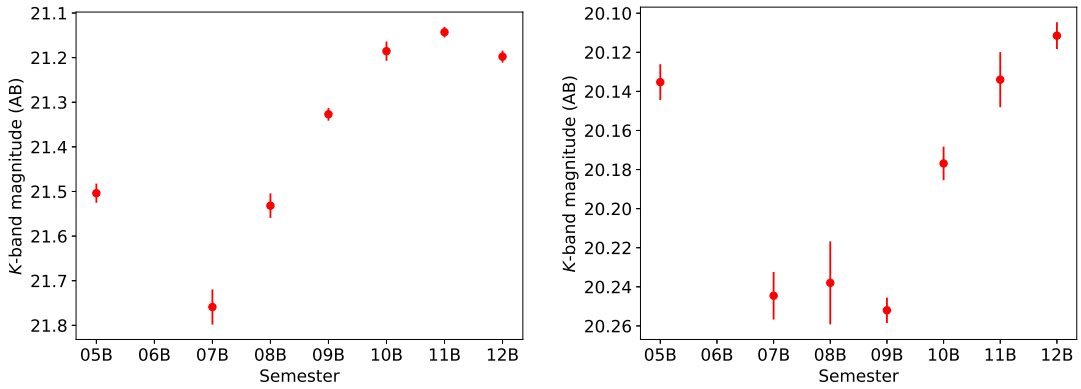

Figure 3.10: The K-band light curves for the variable X-ray detected AGN whose spectra are shown in 3.8

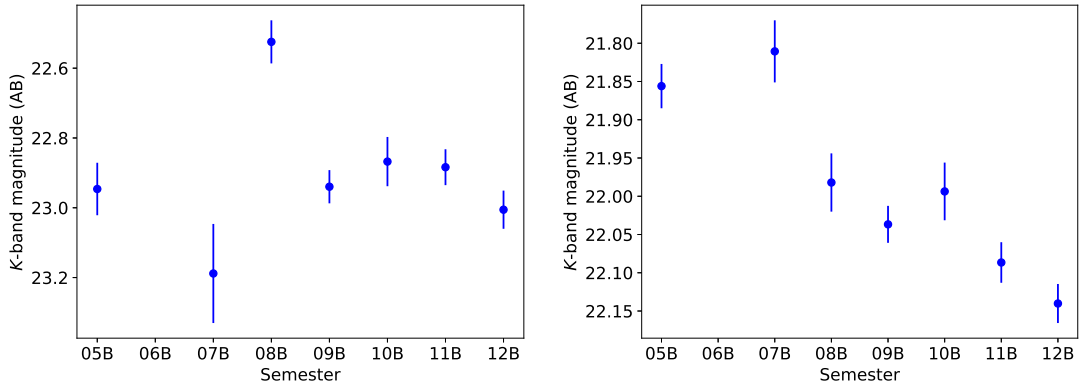

Figure 3.11: The K-band light curves for the variable non-X-ray detected AGN whose spectra are shown in 3.9

have variable light curves different?

From looking at the same colour plots discussed in Section 3.2.1 (Figures 3.4, 3.6, 3.7), we can see that the NIR-non-variable X-ray sources (black squares) sit separately from the NIR-variable X-ray sources (red circles). Notably, the X-ray NIR-variables in Figure 3.4 are mostly within the Stern wedge, but the NIR-non-variable X-ray sources are spread throughout the galaxy locus. The X-ray sources that are found in the variable sample tend to be high-luminosity sources (Figures 3.2 and 3.3) whose IRAC and optical colours appear to be dominated by the AGN, while the non-variable sources seem to be dominated by light from the host galaxy. While it may seem contradictory that the lower luminosity X-ray AGN are less likely to be found in this variability study, given previous works have found that lower luminosity AGN have higher variability amplitudes (e.g. MacLeod et al., 2010; Kozłowski et al., 2016; Vagnetti et al., 2016), it is likely that signal-to-noise ratio provides an explanation for these trends. The lower luminosity AGN will be fainter and are more likely to be dominated by the host galaxy in the K-band, and therefore the variability from the nucleus will be harder to detect despite the larger amplitudes.

3.3 A new population of AGN?

The new population of LLAGN identified by this variability analysis are relatively faint, therefore there may be concerns that these variations are simply noise, or that the variability indicates a different class of object (e.g. supernovae). In this section we address these potential concerns.

3.3.1 Noise?

While the light curves of low flux objects in the survey are noisier, the self-calibrated uncertainties applied to the data in the analysis (Section 2.2.1.4) mean that any increase in noise at low fluxes is accounted for in the uncertainty. In addition, the threshold for the variability selection was chosen such that only 6 false positives are expected across the whole sample, so the entire contamination from false positives is less than 2%.

3.3.2 Supernovae?

One other source of variability is supernovae. As the timescale for supernova events is less than one year, we can identify them by finding sources that only vary in a single epoch. To find these, a secondary analysis was run where we removed the most deviant point of the light curve (i.e. the furthest from the mean) and then recalculated χ^2. We identified those sources that had a $< 99.9\%$ chance of being truly variable (i.e. $\chi^2 < 15.09$) after the removal, and checked these by eye to see if there was truly one flux value that was very different to the rest of the light curve. Fifty sources that had one significantly different epoch were identified, including one definite SN event at $z \sim 2$ (Figure 3.12). Removing these objects does not significantly change the mass and luminosity distributions, and therefore we conclude that these light curves with

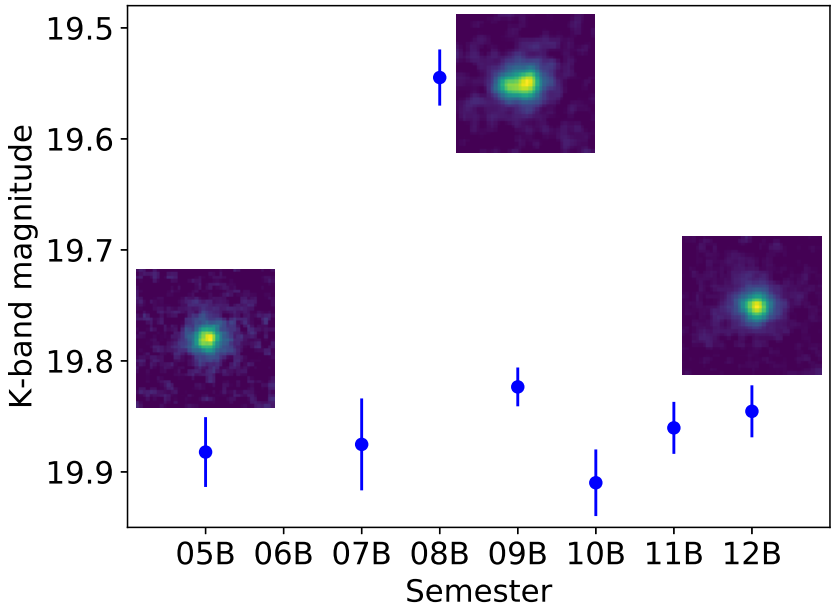

Figure 3.12: Light curve for a potential supernova within the variable sample. The inlaid images show the source before, during and after the flare, which can be seen as a separate object to the left of the galaxy.

anomalous epochs are not driving the trend for variability selected AGN to be found at lower masses and luminosities.

3.3.3 Low-Luminosity AGN?

As we have ruled out the population being down to noise or supernova contamination, the most plausible explanation is that they are LLAGN. This explanation is reinforced by looking at the luminosities of the sources in X-rays, optical and the NIR (Figures 3.2 and 3.3). These figures clearly show that the variable non-X-ray detected sources have systematically lower luminosities in all three regimes.

In addition, LLAGN are expected to have higher amplitudes of variability than high luminosity AGN. Studies in the X-ray regime (e.g. Lawrence & Papadakis, 1993; Almaini et al., 2000; Vagnetti et al., 2016) and in the UV/optical (e.g. MacLeod et al., 2010;

Kozłowski et al., 2016) show that the amplitude of variability is anti-correlated with the luminosity of the AGN. LLAGN have also been found using long-term variability selection methods in the optical and X-ray regimes (e.g. Sánchez-Sáez et al., 2019; Young et al., 2012), therefore it is perhaps not surprising that highly variable LLAGN are found among the low-mass host galaxies in this survey.

3.4 Summary

A comparison to other selection methods showed that only a subset of the variability selected AGN are found in the X-ray (41%) and Stern (48%) selected AGN samples. Within the region of the field imaged with Chandra, those X-ray AGN that are variable tend to be in high mass, high luminosity hosts whose optical and IR light is dominated by the AGN. In contrast, the variable AGN that are not detected in Chandra have lower masses and luminosities, and are dominated by the host galaxy.

We have accounted for any potential contamination of the sample of variable AGN due to noise or supernova events. In preparing the data, we removed any variations due to PSF changes between epochs by convolving the images to match the PSF of the worst image, and incorporated any contribution from noise within the self-calibrated photometric uncertainties. Light curves containing the pattern of variability expected in supernovae were identified through the secondary χ^2 analysis, where the most deviant point was removed from each light curve. When these potential supernovae were removed from the sample, the mass and luminosity distributions of the variable, non-X-ray detected AGN remained lower than those of the X-ray AGN.

Our work builds on studies that select AGN through their optical variability (e.g. Sánchez-Sáez et al., 2019; Pouliasis et al., 2019; De Cicco et al., 2019), but offers the unique ability to study rest frame optical variability at high redshifts ($z > 2$), and

potentially dust-obscured AGN that may be missed by optical selection. Further follow up of the AGN identified in this study will allow a more detailed comparison.

In summary, we find that selecting AGN through just their NIR variability finds a population of low-mass, low-luminosity, X-ray quiet AGN that would be missed by conventional selection techniques, even deep Chandra imaging, as the variability selection probes a wider range of masses and luminosities. Studying this population further will allow us to develop our understanding of the structure of AGN across this wide range of luminosities. We have also found that NIR variability can help us discover peculiar AGN, such as the BAL quasar shown in Figure 3.9.

Chapter 4

Investigating AGN Selected Using Long-term J-band Variability

One of the biggest advantages of the Ultra Deep Survey (UDS) is that we have photometric coverage over 8 years in the J-band as well as the K-band. In this chapter we will discuss how we extended the analysis to select variables in the J-band, and how the resulting variable AGN compare to those selected using the K-band. This will allow us to investigate how the properties of the AGN and the host galaxy can influence whether variability is detected in a particular band.

4.1 Introduction

It is well understood that AGN selected in different wavelengths have different characteristics (see Padovani et al., 2017, and references therein). As such, it would be interesting to investigate if the method for selecting AGN based on long-term variability in the K-band UDS images presented in Chapter 2 could also be applied to the J-band images. The J-band is an interesting region to study as it will probe a region closer to the centre

of the AGN than the K-band, while still probing both the restframe near-infrared at low redshifts and optical light at higher redshifts.

Naively, one might expect to detect the same AGN in the J-band, given that AGN variability is thought to propagate outwards towards longer wavelengths. A comparison of the populations detected at these different wavelengths could therefore test our understanding, both of AGN selection and the physics driving the variability. For instance, if an AGN has significant variability in the K-band but not the J-band, this could suggest that the AGN is dust obscured and the J-band light is too suppressed to detect any variability. We will only be able to identify and investigate objects such as these by comparing the AGN selected through variability in multiple wavebands. In addition, if we also find X-ray quiet AGN in low-mass, low-luminosity hosts using the J-band light curves, such as those found in Chapter 3, this will strengthen the argument that the NIR is a particularly interesting region in which to be completing AGN variability studies.

In this chapter, we first explain the refinements made to selection method following the publication of Paper I in Section 4.2, then we repeat the comparison to X-ray AGN in Section 4.3, before finally comparing the AGN selected in the J-band to those selected in the K-band.

4.2 Selection Method Refinements

In this Chapter, we slightly modified the selection method outlined in Section 2.3. First, we updated the stars catalogue to the latest DR11 catalogue (see Almaini et al., in prep), which extended star selection to fainter magnitudes. This led to 8275 stars being removed from the catalogue, $\sim$ 3000 more than in Chapter 2. None of these additional stars were within our original sample of K-band selected AGN. In addition, we imposed an extra condition ($-0.7 < K_{2arcsec} - K_{0.5arcsec} < -0.5$) on the shape of the stars used to

create the point spread function (PSF) images to ensure that only point-like unsaturated stars were included when optimising the convolution kernels. These changes led to an improved sample of 392 K-band selected variable AGN, 347 of which were also in the sample presented in Chapter 2.

In addition, the 2006B semester had sufficient observations in the J-band, and therefore did not have to be excluded from the variability analysis. This led to J-band light curves with a total of 8 epochs. We once again used a χ^2 fit of the data to a non-varying model to determine the probability than a source is variable, but the additional epoch meant that the analysis now had 7 degrees of freedom rather than 6. In order to be consistent with the K-band analysis, the χ^2 threshold used to select variables in the J-band was chosen to have the same p-value as $\chi^2 = 30$ with 6 degrees of freedom, hence the selection threshold in the J-band is $\chi^2 > 32.08$. The resulting distribution of χ^2 versus J-band flux is shown in Figure 4.1. This analysis gave a sample of 472 J-band selected variable AGN.

After a visual check of these candidate AGN, we uncovered some contamination from cross-talk images (false images created by the readout electronics after bright objects have been observed). The UDS DR11 catalogue identifies all possible cross-talk locations and excludes those most likely to contaminate a galaxy measurement (see Almaini et al., in prep), but we needed to impose more stringent cuts as cross-talk images are likely to vary and therefore contaminate our analysis. We excluded all variables within 2 arcsec of an identified cross-talk artefact where the predicted magnitude of the cross-talk was $> 10\%$ of the magnitude of the variable object. This excluded 25 of the K-band sample and 71 of the J-band sample. Therefore, the final variable AGN samples are 367 K-band selected and 401 J-band selected sources. The changes to the K-band sample did not substantively change the results presented in Chapter 3.

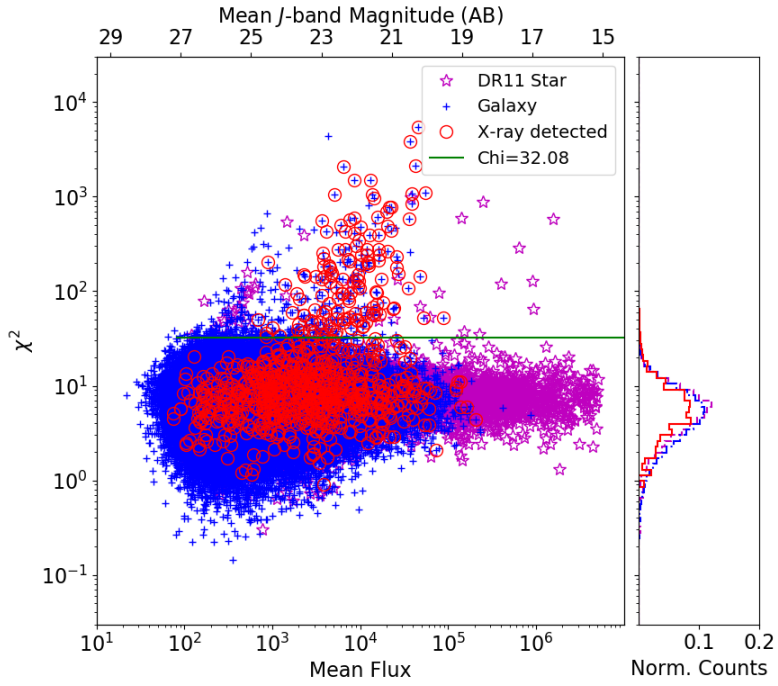

Figure 4.1: χ^2 against mean J band flux for all the objects in the UDS field that are observed in all 8 semesters; the green line indicates the selection threshold.

4.3 Comparison to X-ray AGN

As an initial analysis of these new J-band selected variable AGN, we repeated the comparison of X-ray and variable AGN presented in Chapter 3. We once again restricted the sample to the region imaged with Chandra, which left 182 variables of which 67 (37%) were in the Chandra catalogue. This is a comparable percentage to that found in the K-band (42%). Figure 4.2 shows that the J-band analysis also finds a population of low-mass AGN not seen in X-rays. In addition, Figure 4.3 shows that the variable non-X-ray AGN once again have generally lower luminosities than either the variable X-ray AGN or the non-variable X-ray AGN, and the IRAC colours (Figures 4.4 and 4.5) are also similar to their K-band equivalents (Figures 3.4 and 3.7). Finally, Figure 4.6 shows that the J-band variable AGN are also systematically more X-ray quiet than the X-ray AGN.

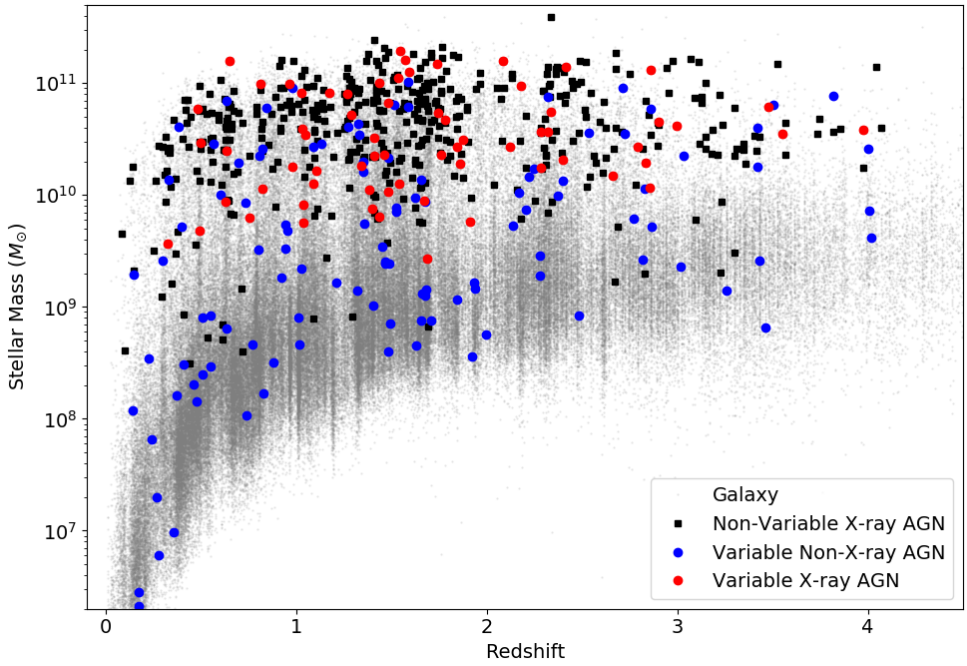

Figure 4.2: Stellar mass distribution with redshift for J-band variables in Chandra region. This is the same as Figure 3.1 but for the J-selected variables.

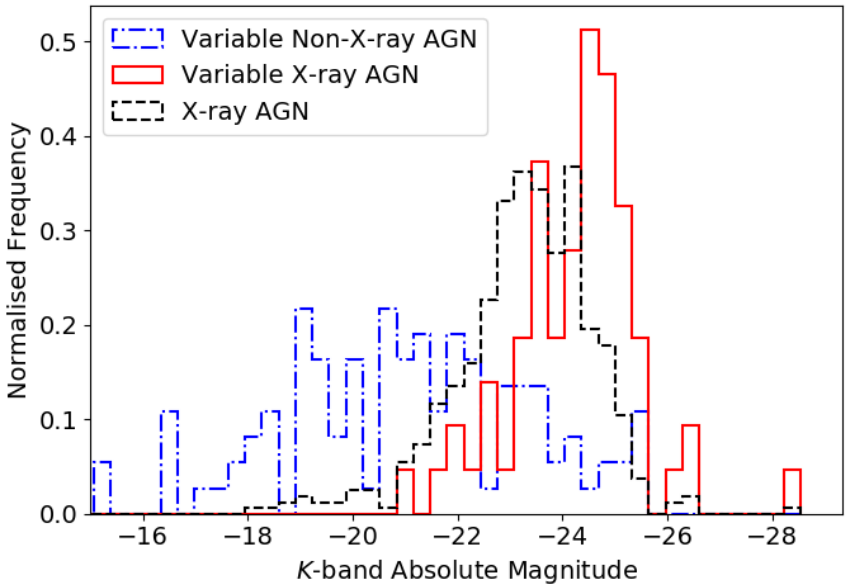

Figure 4.3: Normalised K-band absolute magnitude distributions for J-band variables in the Chandra region. This is the same as Figure 3.3 but for the J-selected variables.

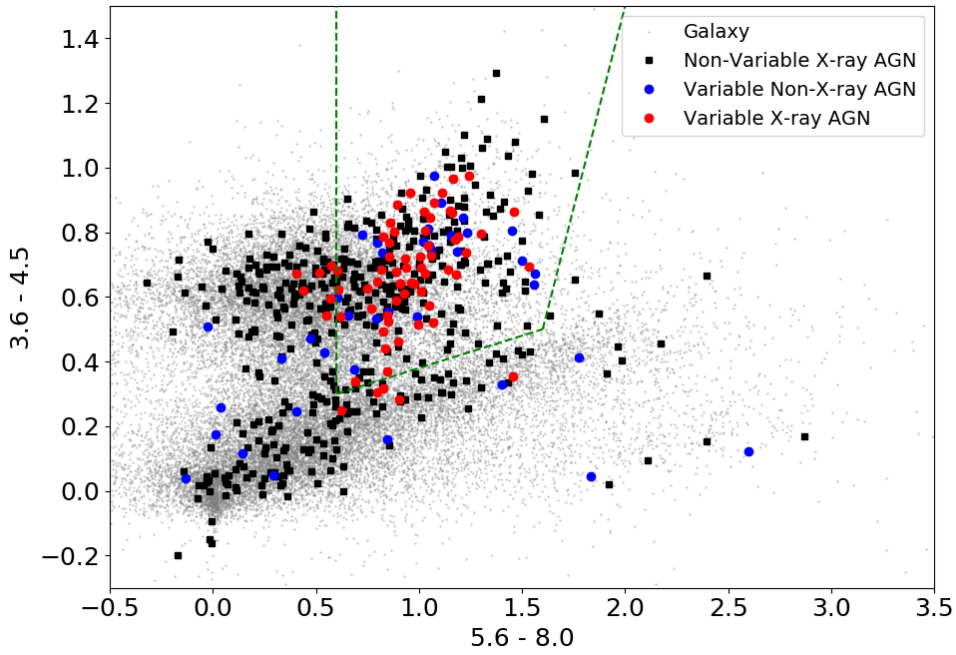

Figure 4.4: AGN selection plot using mid-infrared colours for J-band variables, based on the method of Stern et al. (2005). AGN are known to sit within the wedge indicated by the green dashed line at low redshifts. This is the same as Figure 3.4 but for the J-selected variables.

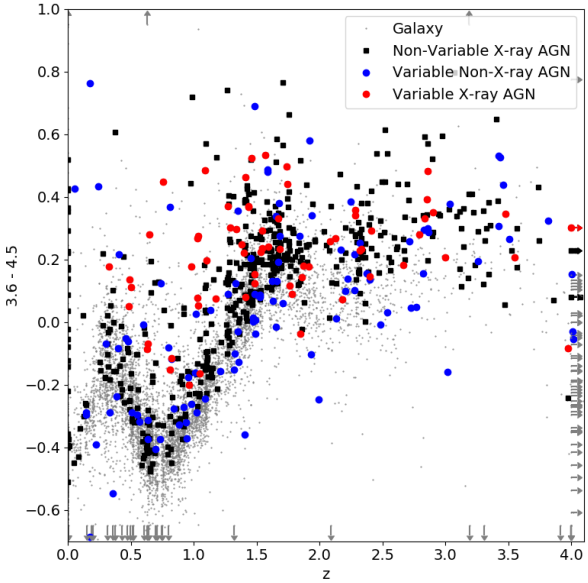

Figure 4.5: 3.6 - 4.5 micron colour as a function of redshift for the J-band variables. AGN usually sit above the galaxy locus in this space. This is the same as Figure 3.7 but for the J-selected variables.

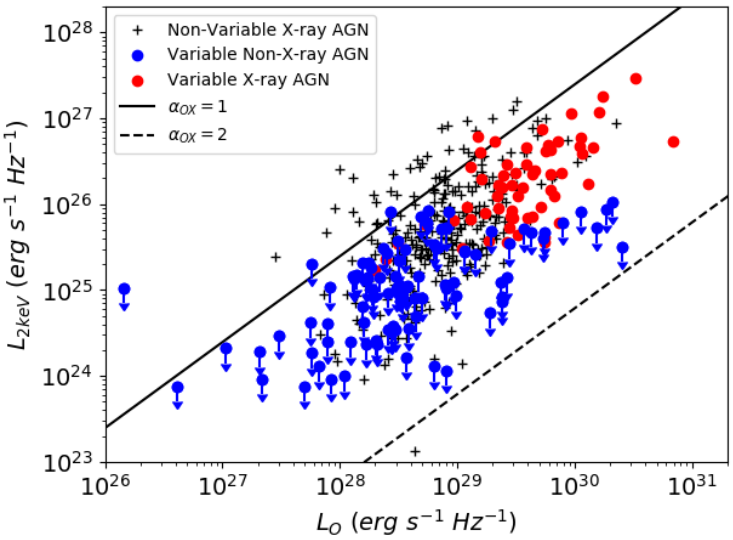

Figure 4.6: Monochromatic X-ray luminosity at 2 keV against monochromatic optical luminosity at 2500 Å for the J-band selected variables. The solid line indicates where $\alpha_{OX} = 1$, and the dashed line shows $\alpha_{OX} = 2$, where α_{OX} is the point-to-point spectral slope between 2 keV and 2500 Å in the restframe. The X-ray luminosities for the non-X-ray detected variable sources are upper limits, as indicated by the blue arrows. This is the same as Figure 3.2 but for J-selected variables

These results are all comparable to the K-band results, and show that selecting AGN based on long-term J-band variability also finds X-ray quiet AGN in low-mass, low-luminosity host galaxies.

4.4 Comparison to K-band Selected Variable AGN

Now that we have a sample of variables that were selected in the K-band and a sample selected in the J-band it would be interesting to investigate if there is anything systematically different about the populations each band selects. If we combine the two datasets, we have a total of 595 variables. In this section we will compare three populations; those that are only selected as variable in the J-band (230), those selected as variable in the K-band (188), and those that are variable in both the J- and K-bands (177), this

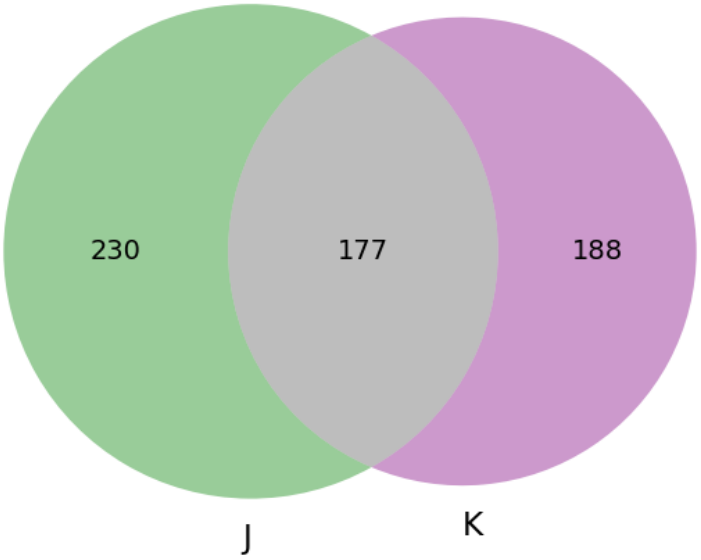

Figure 4.7: Venn Diagram of Selection Band Populations

split is visualised in Figure 4.7.

While we have shown that in both bands the variability selection finds AGN in low-mass host galaxies, Figure 4.8 shows that the 3 populations sit in slightly different regions when stellar mass is plotted against redshift. To examine this difference more closely, Figure 4.9 shows stellar mass histograms in four redshift bins, and it is clear from these that the J-band selected variables have lower mass host galaxies on average than either the K-band or both bands samples across the full range of redshifts. In particular, at low redshifts ($z < 1$) there is a population of high-mass (stellar mass $> 10^{10} M_{\odot}$) variables that are mainly selected in the K-band or both bands but not in the J-band.

These mass differences imply that the AGN selected as variable in different bands have different properties. To investigate this further, we first looked at the available spectra for the variable AGN. Unfortunately, we only have access to spectra for 21 of the variable AGN, which comprises 12 selected in both bands, 7 selected in just the K-band, and 2 selected in the J-band only. These spectra are shown in Figure 4.10.

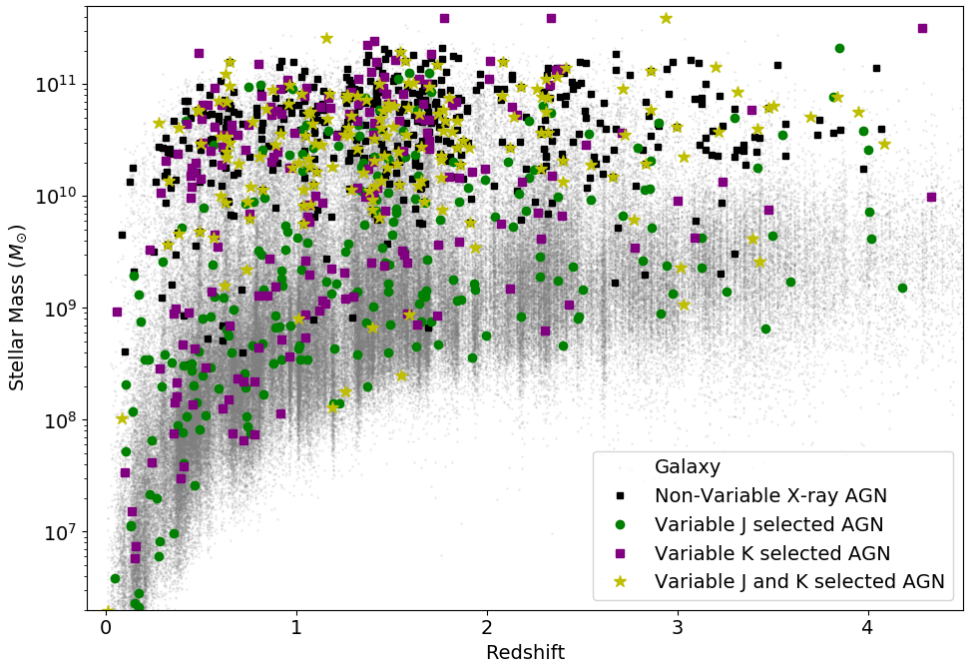

Figure 4.8: Stellar mass - redshift plot with the selection band samples indicated.

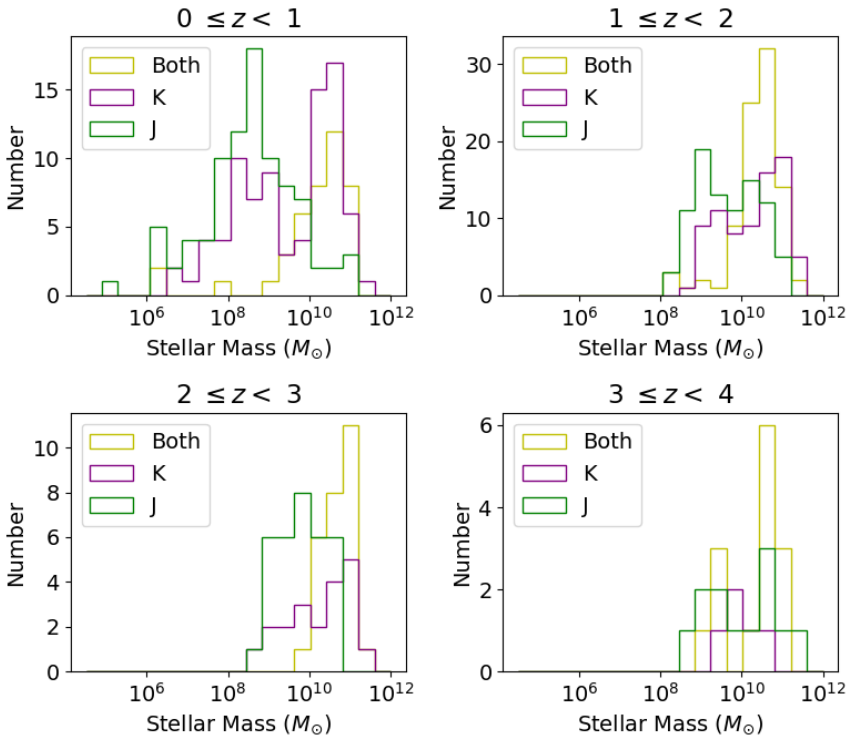

Figure 4.9: Stellar mass distributions for selection band samples in redshift bins.

From visual inspection, we can see that the variables selected in both bands tend to show the strong broader emission lines that are typically associated with quasars, and the K-band selected population tend to have weaker narrow lines or standard galaxy spectra. The two J-band spectra have few distinguishing features; one is at a redshift where there are few lines to detect ($z = 1.53$), while the other ($z = 3.98$) appears to be galaxy dominated.

While the spectra showed a tantalising hint that there is a fundamental difference between the AGN selected in each band, there were only a small sample of spectra available, so we needed to look for confirmation using photometric diagnostics. In Figure 4.11, we show that the three sets of variable AGN sit in different regions of a restframe UVJ colour-colour diagram, which is commonly used to differentiate passive and star-forming galaxies. The J-band selected group are mostly found at the bottom left of the diagram, suggesting that they are primarily hosted by blue star-forming galaxies. The AGN that are variable in both bands sit below the star-forming region, on average, and are where we would expect to find quasars (i.e. AGN dominated SEDs, which are very blue in U-V). Finally, the K-band selected group are scattered throughout the regions where you would expect galaxies to sit, with more galaxies in the region where you find passive galaxies and dusty star-forming galaxies (towards the top) than either of the other two samples.

We know that the objects we have selected are likely to have light with a significant AGN contribution, as this is what allowed us to detect their variability, but this could affect where the host galaxies sit on a UVJ diagram. As such, we wanted to investigate if the position of a host galaxy changes if the aperture size used to calculate the magnitude is changed. Unfortunately, it was not possible for us to do this for the UVJ diagram, as the restframe magnitudes in the UDS DR11 catalogue were only calculated for one aperture size, therefore we used a BzK diagram (Lane et al., 2007; Daddi et al., 2004)

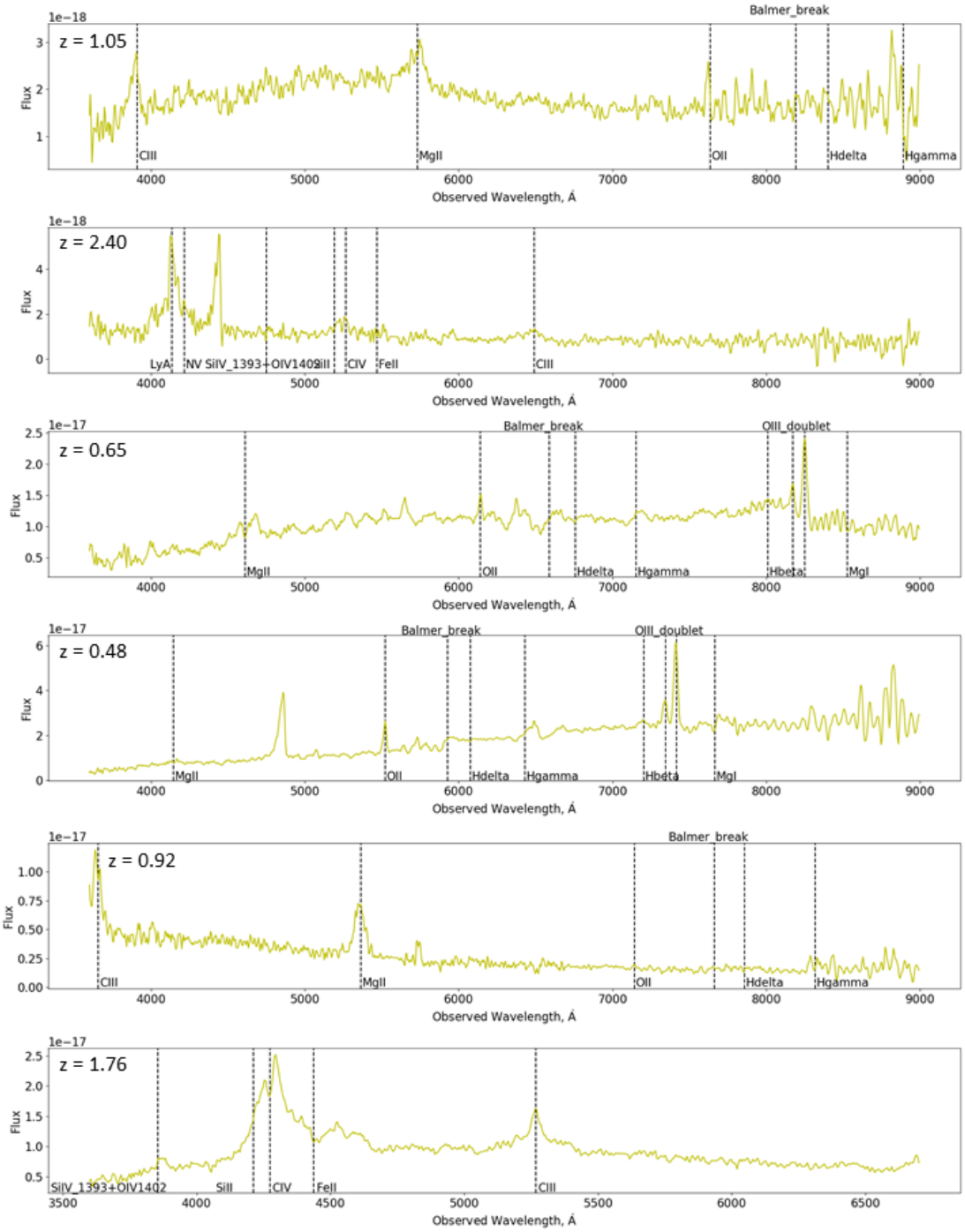

Figure 4.10: VIMOS and FORS2 spectra for the variable AGN. Redshifts are shown in the inset text. Yellow indicates the AGN was selected in both bands, purple indicates selection in the K-band, and green indicates selection in the J-band.

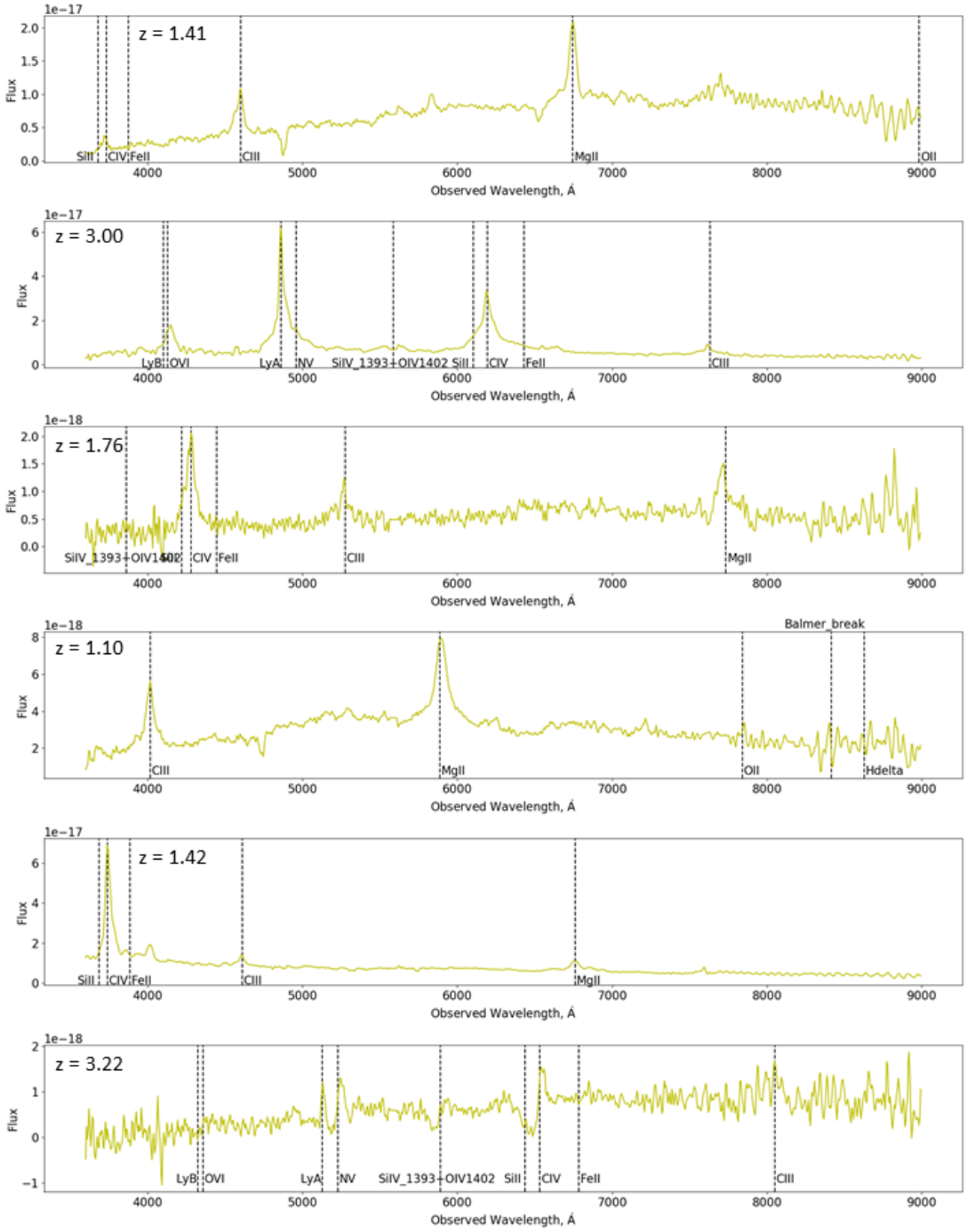

Figure 4.10 (cont.)

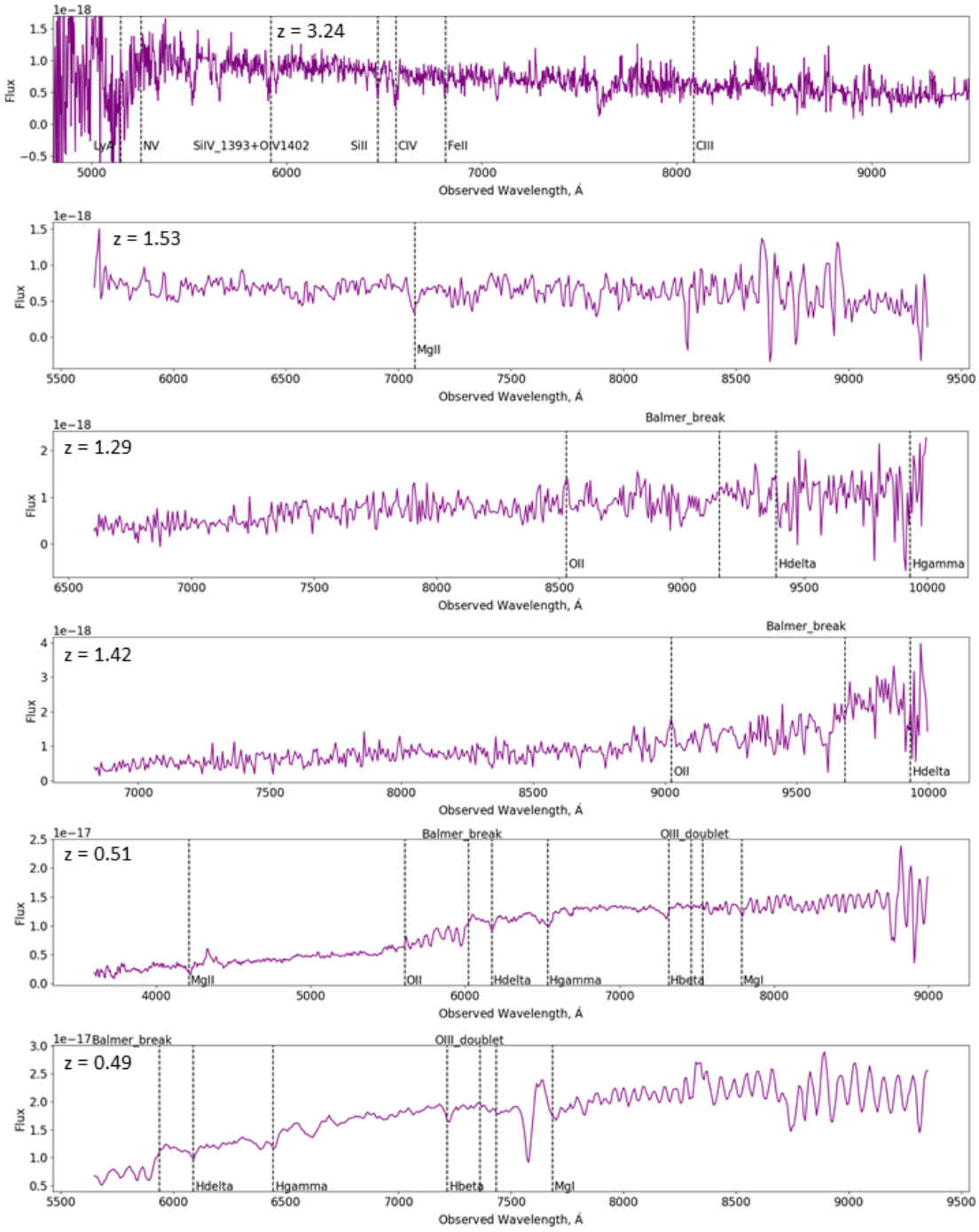

Figure 4.10 (cont.)

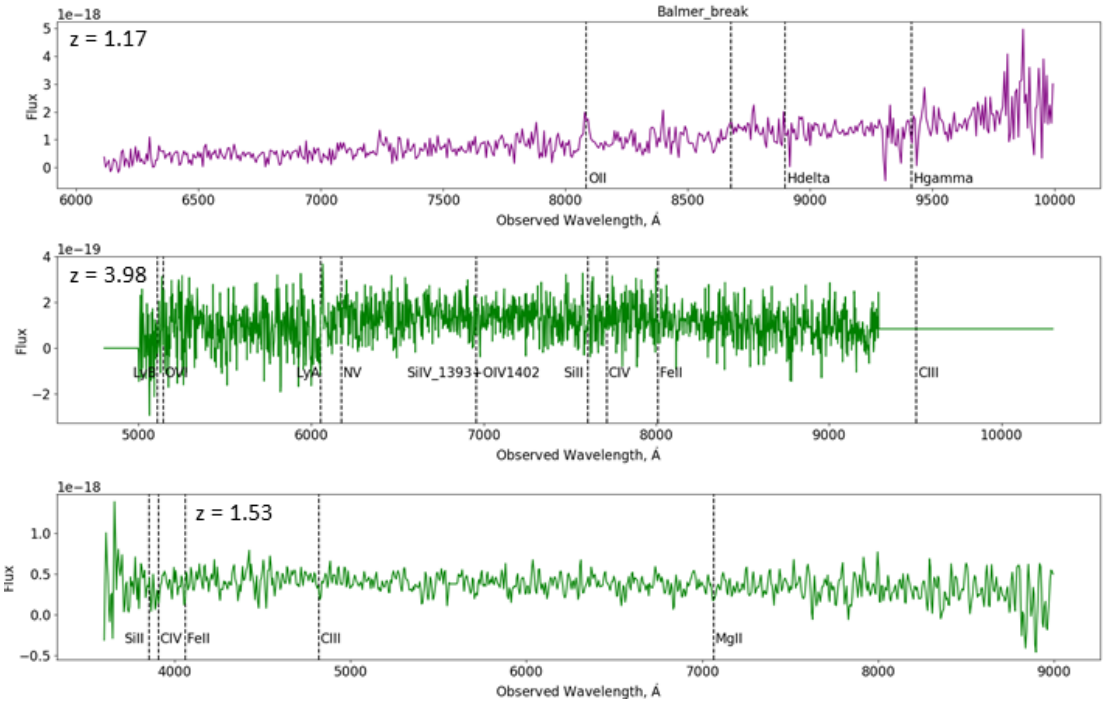

Figure 4.10 (cont.)

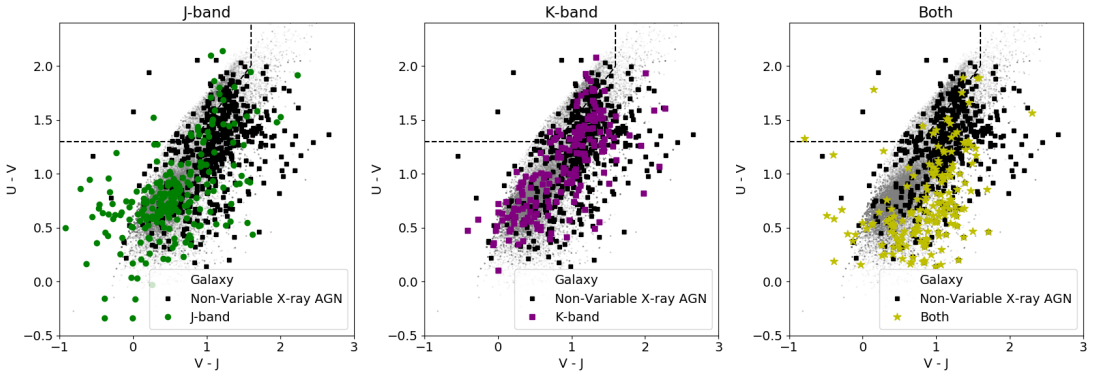

Figure 4.11: Restframe UVJ colour-colour diagrams for each of the three populations. These diagrams are typically used to differentiate quiescent and star-forming galaxies, with quiescent galaxies expected to lie in the top left of the diagram, as indicated by the dashed line.

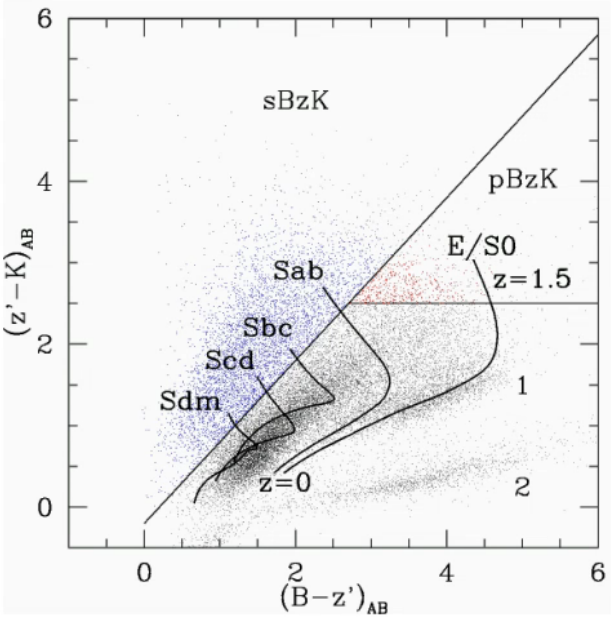

Figure 4.12: Explanation of the BzK diagram taken from (Lane et al., 2007). For above z=1.4, sBzK indicates the region where star-forming galaxies sit, while pBzK indicates where passive galaxies can be found. The tracks are for the model SEDs, branch 1 is where passive galaxies at low redshift sit, branch 2 is the stellar branch.

which can differentiate passive and star-forming galaxies using apparent magnitudes. An example BzK diagram in shown in Figure 4.12 (taken from Lane et al., 2007), where the dividing lines indicate the regions star forming (sBzK) and passive (pBzK) galaxies at $z > 1.4$ sit and the tracks show how galaxies evolve with redshift in this colour space; the track labelled E/S0 is of particular interest as it shows where we would expect to find passive galaxies. Figure 4.13 shows the BzK diagram for each of the samples of variables; the aperture size used increases as you move down the sub-plots. It is noticeable here that the *K*-band selected population once again have more host galaxies in the passive regions of the diagram, and as the aperture size increases more galaxies move onto the passive galaxy track. This change with aperture size shows that the light from the centres of these galaxies is dominated by the AGN emission.

This is further evidenced when we plot a BzK diagram where the magnitudes are

determined from the difference between the flux in the smallest aperture (0.7 arcsec) and the flux in the largest aperture (3 arcsec), as is shown in Figure 4.14. Here we can see that there are clearly a larger number of K-band variable sources in the passive regions of the diagram. As the B - z position is a clear indicator of whether a galaxy is on the passive track, we ran a series of KS tests comparing the B - z distribution of the K-band variable sample to the distributions of the J-band variable sources and the sources that are variable in both bands. In both cases the K-band distribution was significantly different with p-values of 1.07×10^{-8} and 3.75×10^{-6} respectively. It is also worth noting that the K-band B - z distribution was also significantly different from the underlying distribution of galaxies (p-value of 1.16×10^{-13}), while the J-band variable and those variable in both bands were not significantly different from either each other or the underlying galaxy population. These tests show that the K-band variable sources are sitting in host galaxies that occupy the more passive regions of the BzK diagram.

4.5 Discussion

From combining the samples of AGN selected through long-term J- and K-band variability, we have identified three populations of AGN; those selected in both bands, those selected just in the J-band, and those selected in just the K-band. One explanation for the different populations could be that there is a natural spread in variability amplitudes in the sample; some AGN will vary more in J than K and vice versa. To test if there is a distribution of variability amplitudes around a $\sigma_J = \sigma_K$ relationship, where σ is the amplitude of variability in the indicated band, we computed variability amplitudes using the maximum likelihood method described in Almaini et al. (2000). Figure 4.15 shows these amplitudes of variability for the three samples of variable AGN. On average, the AGN vary more in the J-band than the K-band, as you would expect from the reprocess-

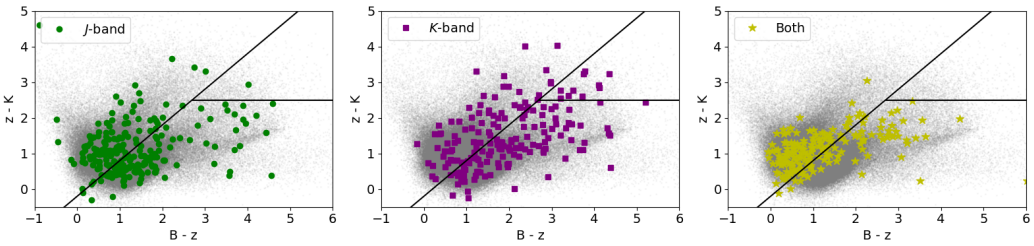

(a) 0.7 arcsec aperture

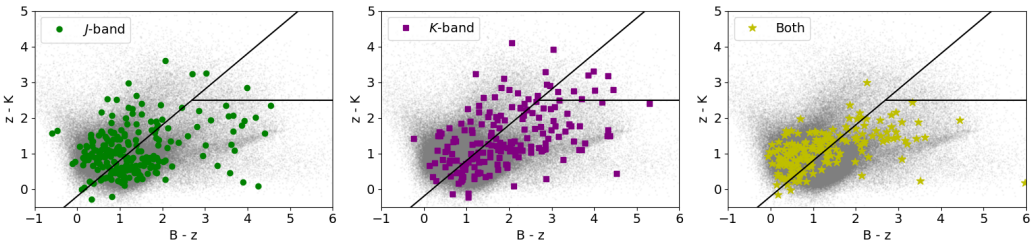

(b) 1.0 arcsec aperture

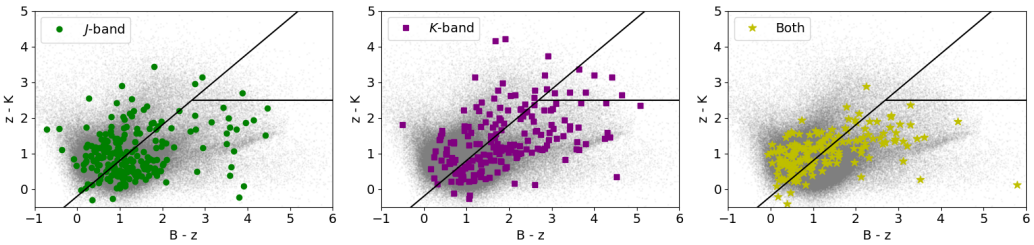

(c) 1.5 arcsec aperture

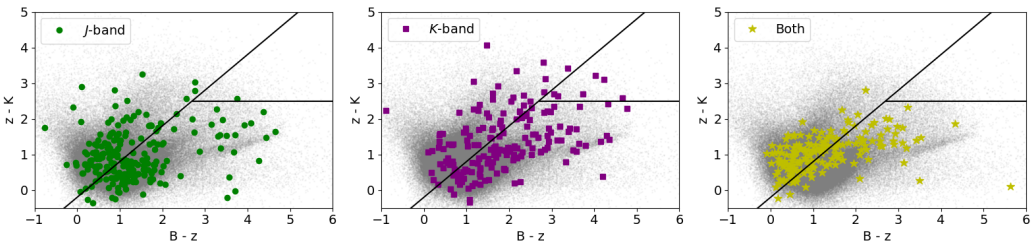

(d) 2.0 arcsec aperture

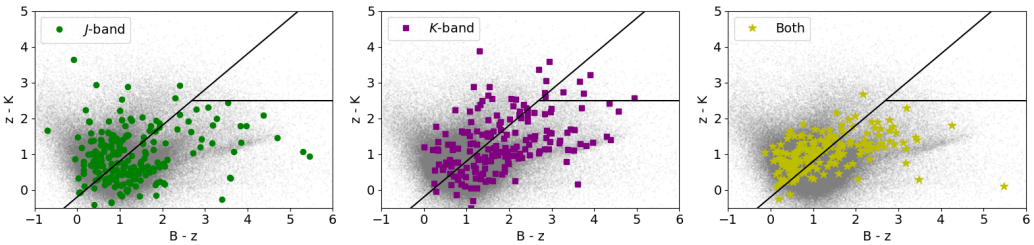

(e) 3.0 arcsec aperture

Figure 4.13: BzK diagrams for the three populations. Aperture size increases from (a)-(e).

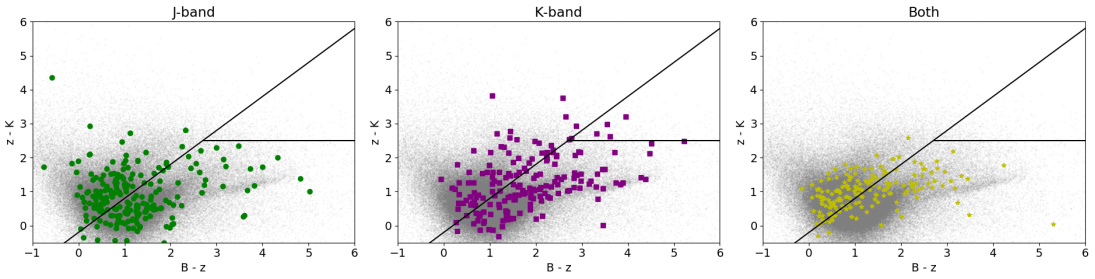

Figure 4.14: BzK diagrams for the three populations. In this version the magnitudes were calculated using the difference between the largest aperture (3 arcsec) and the smallest aperture (0.7 arcsec). This should remove the majority of the AGN contamination.

ing model as amplitudes decrease as wavelength increases. The J-band sample clearly have higher amplitudes in J and, on average, the K-band sample have larger amplitudes in K, as expected. From these amplitude comparisons it would appear that the different populations are just due to selection effects, as some AGN naturally vary more in one band than the other, but the observational differences presented in Section 4.4 suggest that there are some fundamental differences influencing what band the AGN are selected in.

A potential explanation is that a subset the AGN that only vary in the K-band are in dusty host galaxies. The dust in these host galaxies would absorb the J-band light, obscuring any variability. This hypothesis is supported by Figures 4.11, 4.13, and 4.14 which all show the K-band selected variables in the dusty and passive regions. Helpfully, the UDS has also been observed in $24\mu m$ using *Spitzer*, therefore we can examine whether the K-band variable AGN do appear dustier.

For this comparison, we restricted the sample to only the brightest ($K \leq 21$) variables as fainter objects would not have *Spitzer* detections. We found that the variables detected in both bands are most likely to be detected in $24\mu m$ (51%), followed by the K-band with 38%, and finally only 25% of J-band detected variable AGN are also detected in the *Spitzer* $24\mu m$ imaging. We suspect that a higher proportion of AGN that vary in

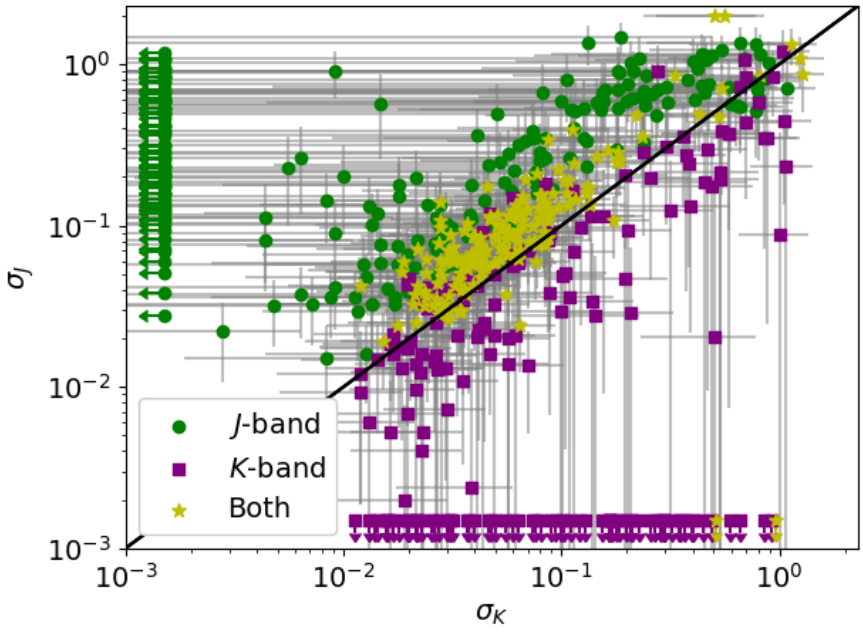

Figure 4.15: Comparison of amplitudes of variability between J- and K-band for the combined variable AGN sample. The variables with amplitudes of 0 are plotted as limits to allow the axes to be shown as log scales. The black line indicates $\sigma_J = \sigma_K$.

both bands are detected in *Spitzer* as these variables tend to be the brightest sources. However, while the K-band are not the most likely to be detected in $24\mu m$, they do appear reddest, as shown in Figure 4.16. This adds weight to the suggestion that variability is not detected in the J-band as this nuclear emission is obscured by dusty host galaxies. This dust must be within the host galaxy, not on AGN scales as the colour diagnostics we have used to reach this conclusion examine the host galaxy colours.

4.6 Summary

In this chapter, we have presented the results from extending our variability selection method to select based on long-term J-band variability. We showed in Section 4.3 that the J-band selected sample produces similar results to those presented in Chapter

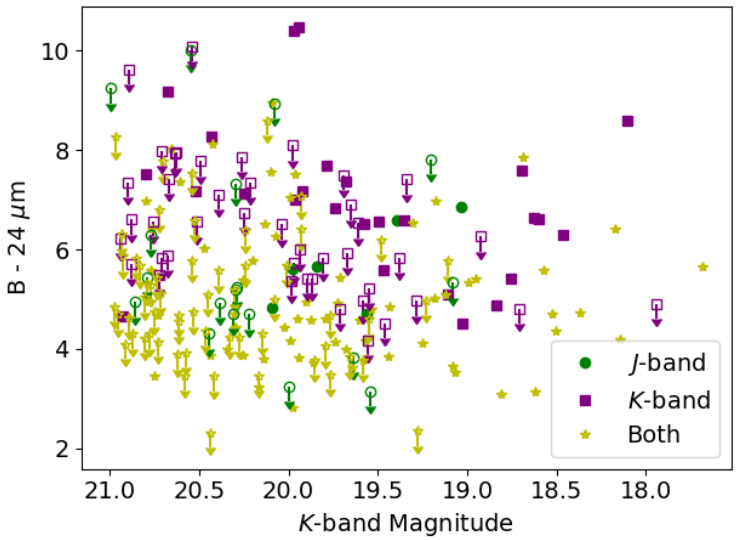

Figure 4.16: B-band magnitude - 24μm magnitude against K-band magnitude for the brightest objects ($K \leq 21$) in the three populations of variable AGN. The filled symbols indicate the source has a 24μm detection, the open symbols with arrows indicate that the source is not detected in 24μm and therefore the value has been calculated as an upper limit. The higher values of $B - 24\mu m$ indicate that the source is redder.

3, i.e. that selecting through long-term NIR variability finds a sample of X-ray quiet AGN in low mass, low luminosity host galaxies that would be missed by other selection techniques. However, if we compare the J- and K-band selected samples we find that there are significant differences between the selected AGN.

The variables that are only detected as variable in the K-band are particularly interesting, and analysis suggests that they are hosted in dustier galaxies than those detected either only in the J-band or in both bands. This means that the lack of variability in the J-band could be due to the J-band light being obscured by dust. From this, one would conclude the K-band is a particularly interesting band in which to select AGN using long-term variability as this can find rare populations and potentially obscured AGN. On the other hand, we find significantly more variables using the J-band light curves, most likely due to the higher variability amplitudes in this band. The combined sample should therefore provide the most complete variability-selected sample.

Chapter 5

Infrared lags in the light curves of AGN

In this chapter, we extend the light curve creation outlined in Section 2.2.1 to generate month timescale light curves. We will compare the resulting J- and K- band light curves to determine if the variability is correlated between the bands, in addition to discovering if there are any time delays between the light curves if they are correlated. The work presented in this chapter was published in Paper II.

5.1 Introduction

The central regions of most Active Galactic Nuclei (AGN) are almost impossible to resolve with current observational techniques, so less direct measures have been used to infer information about their structure. In particular, if the emission from the AGN is varying significantly, then delays or "lags" in the variability between different wavebands can be interpreted as arising from the reprocessing of energy emitted near the centre of the AGN, with, in the simplest picture, the lag representing the extra light travel time for the reprocessed emission (e.g. Sergeev et al., 2005; Cackett et al., 2007). If the environment becomes cooler at larger distances from the AGN, one might expect the

lags to become larger when emission is reprocessed to longer wavelengths, as indeed has been observed in quite a number of low-redshift AGN. For example, Arévalo et al. (2008, 2009) investigate lags between the X-ray and optical light curves, while Sergeev et al. (2005) and Edelson et al. (2015) examine optical lags relative to the ultraviolet, uncovering clear evidence for time delays on timescales ranging from hours to days.

It would be very interesting to push such analyses to longer wavelengths, as one might expect any reprocessing in the near-infrared (NIR) to be occurring in the putative outer dusty torus that perhaps joins on to the inner accretion disk (Koshida et al., 2009). Indeed, work that has been done at these wavelengths suggests longer lags between optical and NIR, though the difficulty of such observations and the heterogeneity of the small number of sources observed has yielded lags ranging from a few days (e.g. Lira et al., 2015; Shappee et al., 2014) to months (e.g. Lira et al., 2011; Oknyansky et al., 2014; Koshida et al., 2009). Ideally, one would want a much larger sample of AGN observed homogeneously and at high quality over years in both the infrared and the optical, in order to study this phenomenon systematically across the population.

Fortunately, the United Kingdom Infrared Telescope (UKIRT) Infrared Deep Sky Survey (UKIDSS) Ultra Deep Survey (UDS), provides the ideal data set for a study of this kind (see Chapter 2 for full details on the survey). The survey obtained data in both J and K infrared bands, and over a wide range in redshift ($0.2 < z < 1.2$) these bands correspond to rest-frame optical ($\lambda < 1\mu$m) and near-infrared emission respectively, so comparing the two bands would allow any lag between these wavebands to be measured.

To this end, we have extracted photometry for a sample of variable AGN from the J- and K-band UDS DR11 observations. In Section 5.2 we describe the sample selection and the cross-correlation method used to determine lags. In Section 5.3, we present the detection of a systematic lag in these data, and how it depends on AGN redshift and luminosity. The implications of these measurements are discussed in Section 5.5.

5.2 Data and Analysis

The AGN used in this study were selected based on their variability, using the method described in Section 2.3, where a source is considered variable based on a χ^2 comparison to a non-varying light curve. In the current work we extend the method to both the *J*- and *K*-band data, co-adding images into deep stacks corresponding to eight years of observations. This analysis yielded an initial total of 595 variable sources, 177 of which were identified as variable in both bands. However, this binning is too crude to search for variability on shorter timescales, so we also produced photometry for the AGN based on month-long snapshots. The lower signal-to-noise level of these shorter observations meant that the fainter sources were too noisy for the subsequent analysis, so we imposed a more stringent variability cut than was used in Section 2.3 of $\chi^2 > 100$, leaving a total of 94 variable sources. We have spectroscopic redshifts for 72 of these sources, and used photometric redshifts for the remaining 22 AGN (see Section 2.2). We note, however, that excluding the objects with photometric redshifts has no significant impact on the results presented below.

The Wide Field Camera (WFCAM; Casali et al., 2007) on UKIRT is made up of 4 separate cameras (see Section 2.2) which each produce slightly different quality images. This difference is not significant in the yearly stacks, as it averages out over the number of observations, but it is noticeable on these shorter timescales. Therefore an additional adjustment to the selection method outlined in Section 2.3 as applied in Section 4.2 was required. This step involved dividing the images into quarters and then running the same convolution as described in Section 2.2.1.2 on these quarter images to homogenise this differing image quality. As observations were not evenly distributed over the survey period, the number of observations compiled into the month stacks ranges from 4 to 214 with an average of 36 for the *J*-band and 50 for the *K*-band stacks. The resulting

variety of image depths is accounted for in the estimation of photometric uncertainties (see Section 2.2). Using these calibrated uncertainties, we find that the S/N of an object with an AB K-band magnitude of $\sim$ 22 (the faintest magnitude in the sample) in the month snapshots ranges from 2.7 to 15.8, with a mean S/N of 10.1 in the K-band and 7.2 in the J-band.

The resulting J and K band light curves for one of the brighter sources are shown in Figure 5.1. There is clearly a strong signature of correlated variability in both bands, and even a tantalizing hint of a lag between the two, but when we sought to quantify it using the discrete correlation function (DCF) as described by Edelson & Krolik (1988), there proved to be insufficient signal in the individual light curves to robustly quantify their lags. Fortunately, the linear nature of cross-correlations means that we can add together the DCFs from individual light curves, after subtracting their mean values and normalizing them, to calculate their ensemble properties. The only other adjustment that has to be made is to adjust the individual objects for cosmic time dilation, so each light curve is measured in its temporal rest frame; this adjustment had the collateral benefit of smoothing the temporal sampling in the stacked data, eliminating any possibility of residual systematics from the observational sampling. The errors on the DCF are estimated by bootstrapped resampling of the light curves 1000 times.

If there is a lag between the two light curves, then the peak in the DCF will be offset from zero. To quantify this effect, following Edelson & Krolik (1988), we adopt two measures of the location of the cross-correlation peak. First, we fit a parabola around the highest single value in the DCF to determine the true location of the peak, $\tau_{\rm peak}$, with an error estimated from the bootstrap analysis, as the width of this peak corresponds to the characteristic timescale of variability rather than the error. After experimenting with this fitting, we found that the most robust range to fit this parabola over was -7 to $+7$ months. Second, we calculate the centroid of all points where DCF $> 0.5 \times {\rm DCF}_{\rm max}$, $\tau_{\rm cent}$,

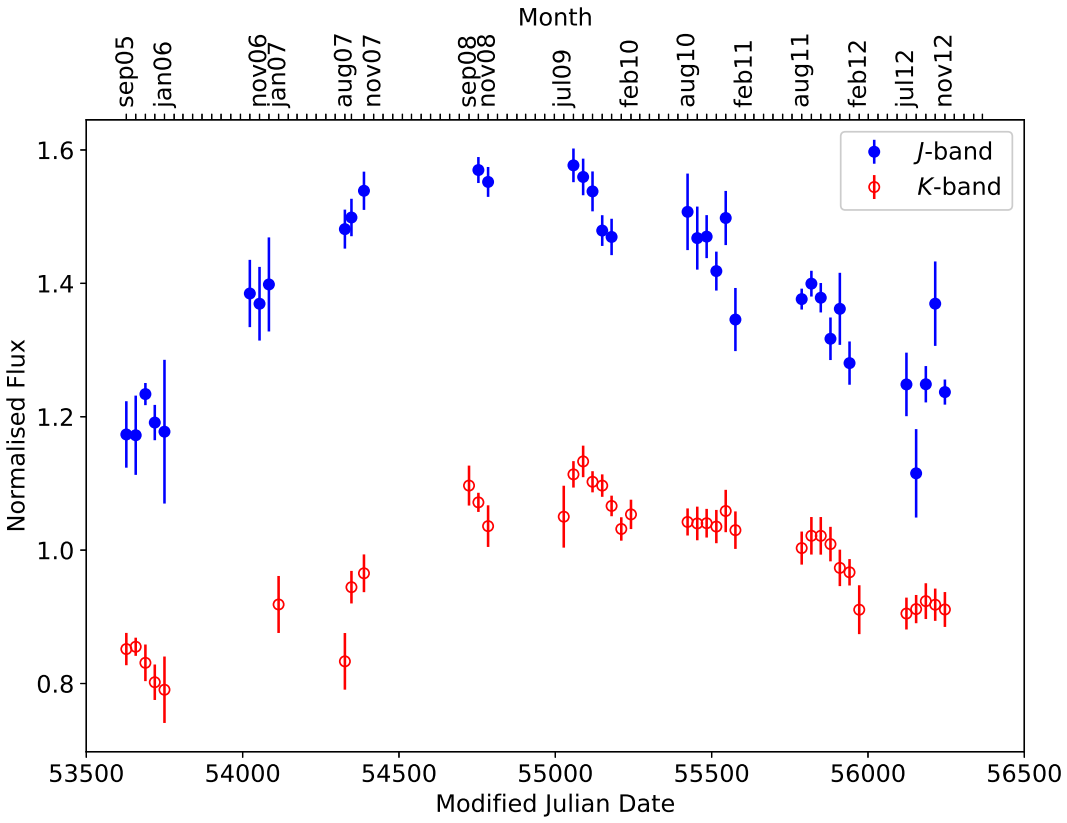

Figure 5.1: Illustrative J- and K-band light curves for an object with high χ^2 variability. The K-band light curve is normalised by the mean flux. The J-band data have been offset by 0.4 in normalised flux for clarity.

with an error estimated from the standard error on this mean value. These quantities are complementary in that if there is any structure in the correlation between the bands, $\tau_{\rm peak}$ is a measure of the modal lag between the two light curves, while the $\tau_{\rm cent}$ measures the mean lag.

5.3 Results

We start with an analysis of the full set of 94 light curves, before going on to subdivide the sources by various criteria (see Table 5.1). The resulting stacked DCF is presented in Figure 5.2. It is apparent that the peak is offset in the positive sense from zero, implying

Subset	Number of Variable AGN
$\chi^2 > 100$	94
$z \geq 1.2$	46
$z < 1.2$	41
$-21.1 > M_K \geq -24.0$	22
$-24.0 > M_K \geq -26.4$	19

Table 5.1: The number of variable AGN used to create the discrete correlation functions shown in Figures 5.2-5.4. The total number in the redshift subsets does not add up to 94 as 7 objects were removed due to large uncertainties in their photo-z estimations.

that the K-band light lags behind that in the J-band, as predicted. Quantitatively, we find $\tau_{\rm peak} = 0.7 \pm 0.2$ months and $\tau_{\rm cent} = 0.9 \pm 0.3$ months, so both metrics are statistically significant at the 3σ level. These results illustrate the well-known strength of cross-correlation analysis in detecting signal at, or even below, the binning level, though we note that cosmological time dilation means that the light curves are actually sampled on significantly shorter timescales.

One effect that we might expect to dilute the signal in Figure 5.2 originates in the wide range of redshifts in the data stacked together. For the lower redshift sources, while the J-band data typically represents optical emission, the K-band comes from the rest-frame infrared, providing the signal we are looking for. However, at higher redshifts, both infrared bands were emitted in the rest-frame optical, for which, as discussed in Section 5.1, lags are shorter. To test for this effect, Figure 5.3 shows the stacked DCFs divided into two, with the division at $z = 1.2$ representing the approximate point at which the observed K-band corresponds to rest-frame optical light ($< 1\mu$m). Indeed, as predicted, the lags are significantly longer in the low-redshift regime where we are comparing rest-frame optical and infrared emission. It is also notable that the low-redshift DCF peak shows a distinct asymmetry with a longer-lag shoulder, which is further emphasized by the difference between $\tau_{\rm peak}$ and $\tau_{\rm cent}$. There is clearly information here regarding the structure of the emitting region, although a detailed analysis of this

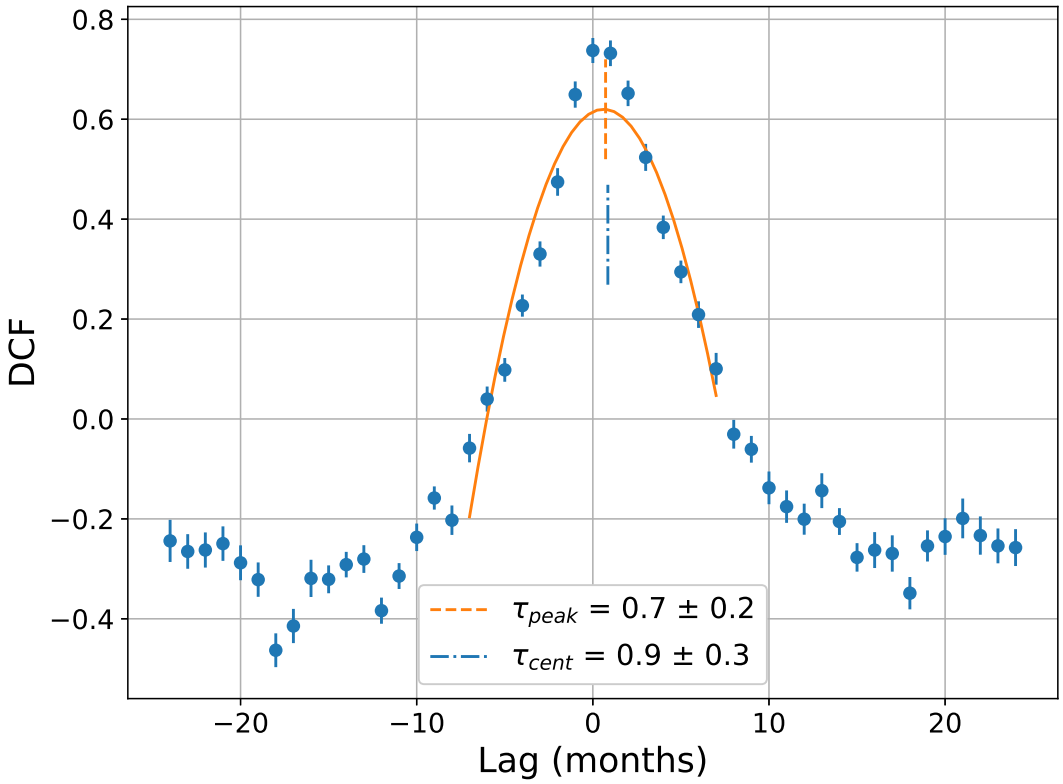

Figure 5.2: The stacked discrete cross-correlation function between J- and K-band data for the 94 AGN selected from the UKIDSS UDS. Two measurements of the characteristic lag are shown (in months). The parabola shows the fit used to calculate $\tau_{\rm peak}$ (shown as an orange dashed line). The blue dash-dot line shows the centroid shift, $\tau_{\rm cent}$.

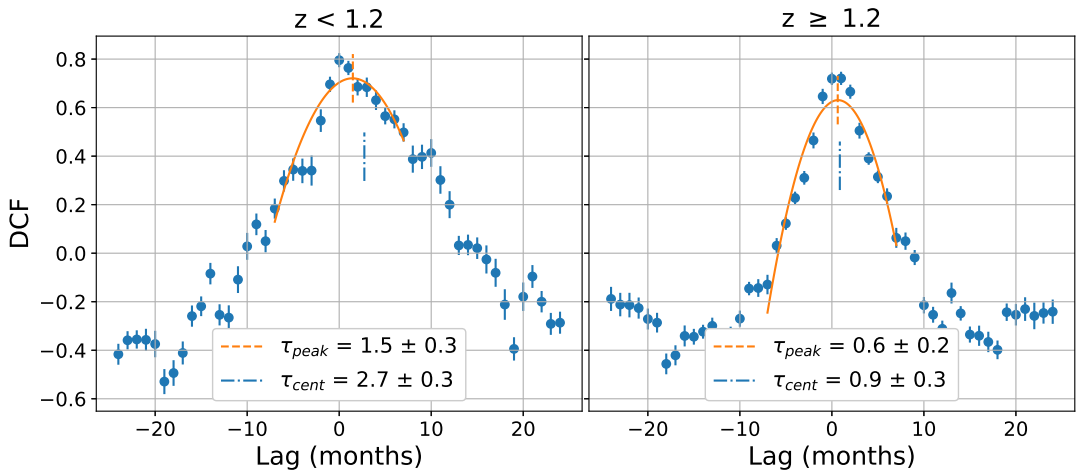

Figure 5.3: The stacked discrete cross-correlation function, as in Figure 5.2, but with the AGN divided into two groups based on whether above or below a redshift of $z = 1.2$. Two measurements of the characteristic lag are shown (in months).

transfer function would require more data.

One further test that we can apply to this analysis comes from noting that one would generically expect that more luminous sources are physically larger, so the lags might be expected to also be larger for the intrinsically brighter sources. Figure 5.4 shows the DCFs obtained when the lower-redshift sources are separated at a K-band absolute magnitude of $M_K = -24$, this divide was chosen as it roughly divides the AGN into equal bins. As is apparent from this figure, the more luminous sources do, indeed, show significantly longer lags, with the asymmetric shoulder discussed above particularly clear in these objects.

Interestingly, however, if we repeat this analysis using just the higher-redshift sources (where we are comparing emission just in the rest-frame optical), we find a lag of ~ 1 month at high luminosities, which is not what we would expect from previous studies of AGN in the rest-frame optical light, which find lags of ~ 1 day (e.g. Sergeev et al., 2005; Edelson et al., 2015). Therefore, the structure is potentially more complicated than the simple picture we have considered here.

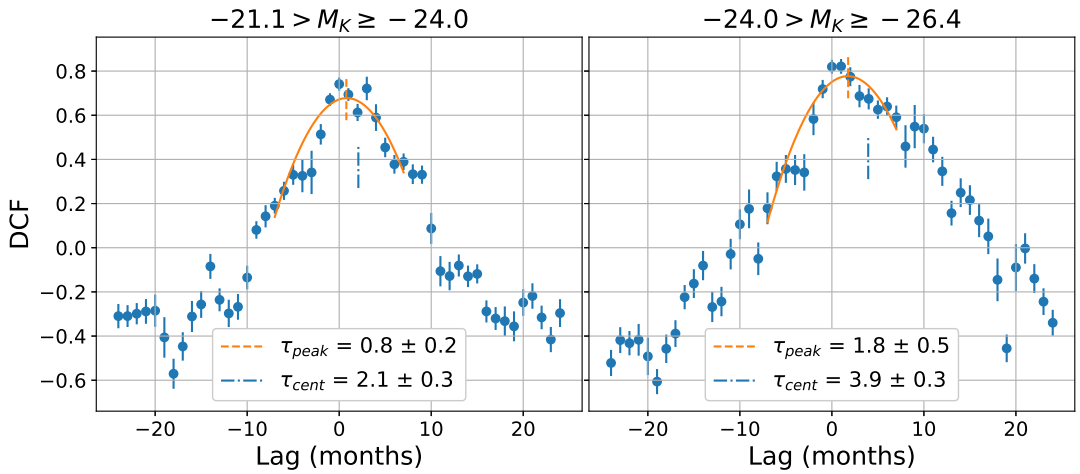

Figure 5.4: The stacked discrete cross-correlation function, as in Figure 5.2, but with the low-redshift AGN divided into two groups based on whether their K-band absolute magnitude is fainter or brighter than $M_K = -24$. Two measurements of the characteristic lag are shown (in months).

5.4 Physical Implications

In order to further understand what physical processes could produce the $\sim$ 1 month lags presented in Section 5.3, we assumed a simple toy model where a central source varies and illuminates a disk radius on light-travel timescales (e.g. Collier et al., 1998). We assume that the disk radiates as a black body, and therefore the temperature of the disk can be determined using Wien's law. The temperature can then be related to a radius using

$$T(r) = 6.3 \times 10^5 \left(\frac{\dot{M}}{\dot{M}_E}\right)^{\frac{1}{4}} \left(\frac{M}{10^8 M_\odot}\right)^{-\frac{1}{4}} \left(\frac{r}{R_S}\right)^{-\frac{3}{4}} \tag{5.1}$$

where r is the radius the emission comes from, $\dot{M}$ is the accretion rate, $\dot{M}_E$ is the Eddington rate, M is the black hole mass, $M_\odot$ is the mass of the sun, and R_S is the Schwarzschild radius. Once the emission radius has been determined for each band (J and K, taking redshift into account), the light travel time between the two radii can be

calculated. If this model is correct, the lag will be the same as the light travel time.

If we assume a black hole mass of $10^7 M_\odot$, an accretion rate of $0.1\dot{M}_E$, and a redshift of 0.5, which is approximately the middle of our low redshift bin, this model would predict lags of 0.046 months. For $z = 1.5$ this reduces to just 0.023 months. Both of these values are more than one order of magnitude away from the measured lags in their corresponding redshift bins. As might be expected, this demonstrates that there is something more complicated occurring to produce lags on month timescales.

Previous studies such as Lira et al. (2011) have studied the light curves of individual AGN in great detail. A significant advantage of these studies is that the properties of the AGN (such as the black hole mass) are known, therefore the modelling can be more precise. While Lira et al. (2011) primarily compares lags between NIR bands and the B band, if we look at the difference between the $B - J$ lag and the $B - K$ lag we can infer that they would see a lag of $\sim$ 35 days between the J and K bands in NGC 3783 (Table 3, Lira et al., 2011). This is directly comparable to our results as NGC 3783 has a black hole mass of $3 \times 10^7 M_\odot$. They attribute this extended lag to two sources, as their DCF peak is extended in a similar manner to the low redshift DCF presented in Figure 5.3; short-term variations that follow the optical variability of the accretion disk, and long-term variations caused by the dusty torus. Models of the dust sublimation radius in NGC 3783 support this theory as the radius is in good agreement with to optical-to-NIR lag length. As NGC 3783 is comparable to our low-redshift sample, we can postulate that the $\sim$ 1 month lags, and the extended structure seen in this DCF peak, is likely to be due to contributions from the dusty torus.

5.5 Summary

There is a wealth of information on the structure of AGN to be found in their light curves, and the lags in variability between wave bands. The near infrared offers a potentially important perspective, as it may probe out to the dusty toroidal region that surrounds an inner accretion disk, but observationally it has proved challenging to study for long enough periods and for a sufficient number sources to learn much about the overall population of AGN. Here we have shown that the UKIDSS UDS offers a different window on this probe: the period over which it was obtained spans the timescales of interest very nicely, while its depth means that, even within its relatively small field, we can detect orders of magnitude more variable AGN than previous studies of individual targets. We have also shown that even where there is not sufficient signal to learn much from individual sources, stacking such consistent data together provides a strong ensemble signal. This analysis confirms that there is, indeed, a significantly longer lag between optical and infrared light than between optical bands, and that the length of the lag increases with the luminosity of the source as we might physically expect.

We also see clear indications of structure in the stacked DCFs, indicating that there is still more evidence to be found in data obtained in this way; the fact that this structure does not average away when derived from such stacked data implies that it is a generic feature of these objects rather than a peculiarity of any particular source. Detailed modelling of this signal, and its implications for AGN structure, is beyond the scope of this work. However, we have demonstrated that there is an interesting signal here that is worth modelling and investigating further. Significant progress in this area requires larger areas or deeper data than the UDS supplies, to beat down the remaining noise in this generic signal, and to allow more nuanced subdivision of the data. Upcoming infrared surveys (e.g. the Euclid deep fields and VEILS: Laureijs et al., 2011; Hönig

et al., 2017) will potentially allow us to do exactly this analysis, but only if it is considered in the survey design, for example in defining how the target region is imaged over time.

Chapter 6

Conclusions and Future Work

Variability has been a known characteristic of AGN since their discovery, although the origins of the variations are still hotly debated. These variations in the light curves of AGN allow us to probe the innermost regions of AGN, and have been successfully used in optical and UV wavelengths to select AGN from survey catalogues. The UKIDSS UDS presents a rare opportunity to investigate whether selecting AGN via variability can also be undertaken in the NIR. The timescale of variability in AGN increases with wavelength, resulting in month-to-year timescales in the NIR, so NIR data must be taken over 5-10 years in order to sample the light curve sufficiently to study AGN variability. In this thesis, we have shown that AGN can be selected through long-term variability in both the J- and K-bands, and that selecting AGN in this way uncovers rare populations of AGN in addition to expanding our understanding of variability mechanisms.

6.1 Conclusions

The NIR is a particularly interesting region in which to study AGN as it probes the rest-frame optical at high redshifts as well as the rest-frame NIR at low redshifts. This

means it has the rare ability to investigate the edges of both the accretion disk and the dusty torus, as assumed in the unified model of AGN. Historically, the NIR has not been well studied as there is dip in the AGN SED at these wavelengths (Figure 1.3), caused by a decrease in light emitted from the accretion disk before the torus emission begins to contribute. In addition, NIR wavelengths are hard to observe as the sky background is orders of magnitude brighter than the optical sky background. However, with a sufficiently deep survey, interesting information can be obtained from these sources even in this less luminous region of its SED. Variability is also a powerful tool to further our understanding of the innermost regions of AGN, and combining these two probes has allowed us to investigate AGN physics in a unique way.

In this thesis, we have shown that the UDS is the perfect survey for selecting AGN through their NIR variability, due to its long baseline of observations and deep imaging. We showed that this could be done in the K-band in Chapter 2, along with the preparation steps required to make sure any variation detected came from the object and was not due to any systematic errors in the data. In Chapter 3, we then discussed how the AGN selected in this manner compared to those selected by more traditional methods, in particular through deep Chandra imaging. We concluded that selecting AGN through only their K-band variability had allowed us to discover a population of X-ray quiet AGN in low-mass, low-luminosity host galaxies, that would have been missed by both deep X-ray imaging and mid-infrared colour selection techniques.

Having established that selecting AGN using K-band light curves is possible, and shown that selecting AGN this way helps us create a more complete census of AGN in the universe, we decided to extend this selection into the J-band. This served the dual purpose of establishing whether the same population could be found using a bluer waveband, and allowing us to compare the sources selected in each band to see if certain AGN vary more in one band than the other. This analysis was discussed in Chapter 4,

where we showed that we find similar X-ray quiet AGN in low-mass, low-luminosity host galaxies, but the host galaxies differed depending on which band the AGN was selected in. In particular, some of the K-band only selected variable AGN seem to be obscured AGN.

Once we had a combined sample of AGN selected in either the J- or K-band, we could then directly compare the variability of the AGN between the bands. In order to make any meaningful comparisons, we first needed more epochs in our light curves. While the semester light curves capture the majority of the long-term variations, we wanted to be able to investigate differences on timescales of approximately one month, as this is the scale where previous studies had found lags between J- and K-band light curves. Therefore, we adapted our data preparation steps to create an epoch for each calendar month of UDS observations. These light curves were sufficiently well sampled for us to run a cross-correlation analysis on our J- and K-band light curves. While there was insufficient signal in any single pair of light curves, running a stacked cross-correlation on the light curves of the 96 variable AGN with $\chi^2 > 100$ showed that the K-band variability lagged the J-band light at all redshifts, but this lag was longer at low redshifts.

These lags are longer than would be expected from a simple model where an accretion disk is illuminated by a varying central source, but are consistent with previous work on NIR inter-band lags at low redshifts. This is the first time that an investigation of this kind has been done on a large enough sample of NIR light curves to show that these long lags occur across a sizeable population of AGN, not just in one or two cases. In previous studies, extended lags were thought to show that the light is at least partly originating in a dusty torus. This discovery has implications for AGN physics, as it may imply an additional delay in reprocessing the light into the NIR emitting dust. There are also hints at underlying structure in the shapes of the cross-correlation functions,

suggesting that further investigations of these cross-correlation results could shed light on the transition from accretion disk to dusty torus. However, a deeper, better sampled survey will be required to robustly investigate these theories.

Overall, this thesis has shown that studying variability of AGN in the NIR provides a new and unique probe of AGN physics. We have shown that we can find AGN that would be missed by other techniques, and that studying the properties of these AGN can develop our understanding of their inner workings, and how the host galaxy can influence how we observe the variability.

6.2 Future Work

The work completed in this thesis was the first to select AGN using NIR variability, and has shown that this offers a new way to investigate AGN physics. There is still a wealth of information available in the UDS data; for instance, we only briefly touched upon examining the amplitudes of variability. In addition, the month light curves created for Chapter 5 could be used to search more systematically for supernovae within the UDS field, similar to the candidate we discovered serendipitously.

A major route in continuing the studies presented here would be to complete spectroscopic follow-up for the majority of the sample. Comparing the spectroscopic classifications of the AGN, depending on the band in which they are selected, could further the observations made in Chapter 4. This follow up would be a non-trivial undertaking as the most interesting sources to observe are the low-luminosity, low-mass objects. These sources will be faint and therefore a large telescope will be required. In addition, a multi-object spectrograph with a reasonably large field of view would be required in order to efficiently observe a large proportion of the sample.

The main point we would like readers to take away from this thesis is that NIR variability is a unique probe of AGN structure, and as such future NIR surveys should be designed with sufficient cadence to investigate AGN light curves. There are hints at details about the structure of the edge of the accretion disk and start of the torus in the DCF functions shown in Chapter 5, but it will not be possible to drill further into this without better sampled light curves over a similar period. Plans for future NIR surveys, such as Euclid, currently include deep fields that will be visited often over a period of a few months, but, in order to develop studies of this kind, these fields need to be observed regularly over a number of years.

Bibliography

Abbott B. P., et al., 2016, Physical Review Letters, 116, 061102

Abbott B. P., et al., 2017, The Astrophysical Journal Letters, 848, L12

Almaini O., et al., 2000, Monthly Notices of the Royal Astronomical Society, 315, 325

Angione R. J., 1973, The Astronomical Journal, 78, 353

Antonucci R., 1993, Annual Review of Astronomy and Astrophysics, 31, 473

Arévalo P., Uttley P., Kaspi S., Breedt E., Lira P., McHardy I. M., 2008, Monthly Notices of the Royal Astronomical Society, 389, 1479

Arévalo P., Uttley P., Lira P., Breedt E., McHardy I. M., Churazov E., 2009, Monthly Notices of the Royal Astronomical Society, 397, 2004

Baade W., Minkowski R., 1954, The Astrophysical Journal, 119, 215

Beckmann V., Shrader C. R., 2012, in An INTEGRAL view of the high-energy sky (the first 10 years). Paris

Bertin E., Arnouts S., 1996, Astronomy and Astrophysics Supplement Series, 117, 393

Bertin E., Mellier Y., Radovich M., Missonnier G., Didelon P., Morin B., 2002, in Astronomical Data Analysis Software and Systems XI.

Blumenthal G. R., Gould R. J., 1970, Reviews of Modern Physics, 42, 237

Bradshaw E. J., et al., 2013, Monthly Notices of the Royal Astronomical Society, 433, 194

Brammer G. B., van Dokkum P. G., Coppi P., 2008, The Astrophysical Journal, 686, 1503

Bruzual G., Charlot S., 2003, Monthly Notices of the Royal Astronomical Society, 344, 1000

Butler N. R., Bloom J. S., 2011, The Astronomical Journal, 141, 93

Cackett E. M., Horne K., Winkler H., 2007, Monthly Notices of the Royal Astronomical Society, 380, 669

Caplar N., Lilly S. J., Trakhtenbrot B., 2017, The Astrophysical Journal, 834, 111

Casali M., et al., 2007, Astronomy & Astrophysics, 467, 777

Collier S. J., et al., 1998, The Astrophysical Journal, 500, 162

Condon J. J., 1992, Annual Review of Astronomy and Astrophysics, 30, 575

Daddi E., Cimatti A., Renzini A., Fontana A., Mignoli M., Pozzetti L., Tozzi P., Zamorani G., 2004, The Astrophysical Journal, 617, 746

De Cicco D., et al., 2019, Astronomy & Astrophysics, 627, A33

Donley J. L., Rieke G. H., Perez-Gonzalez P. G., Barro G., 2008, The Astrophysical Journal, 687, 111

Dunlop J., et al., 2007, Spitzer Proposal ID 40021

Edelson R. A., Krolik J. H., 1988, The Astrophysical Journal, 333, 646

Edelson R., Nandra K., 1999, The Astrophysical Journal, 514, 682

Edelson R., et al., 2015, Astrophysical Journal, 806, 129

Einstein A., 1916, Annalen der Physik, 354, 769

Elvis M., Maccacaro T., Wilson A. S., Ward M. J., Penston M. V., Fosbury R. A. E., Perola G. C., 1978, Monthly Notices of the Royal Astronomical Society, 183, 129

Enya K., Yoshii Y., Kobayashi Y., Minezaki T., Tomita H., Peterson B. A., 2002, The Astrophysical Journal Supplement Series, Volume 141, Issue 1, pp. 31-44., 141, 31

Fath E. A., 1909, Lick Observatory Bulletin, 149, 71

Fazio G. G., et al., 2004, The Astrophysical Journal Supplement Series, 154, 10

Feltre A., Charlot S., Gutkin J., 2016, Monthly Notices of the Royal Astronomical Society, 456, 3354

Finkelstein D., 1958, Physical Review, 110, 965

Genzel R., et al., 1998, The Astrophysical Journal, 498, 579

Gillessen S., Eisenhauer F., Trippe S., Alexander T., Genzel R., Martins F., Ott T., 2009, Astrophysical Journal, 692, 1075

Harrison C. M., 2014, PhD thesis, Durham University, Durham

Hönig S. F., et al., 2017, Monthly Notices of the Royal Astronomical Society, 464, 1693

Kocevski D. D., et al., 2018, The Astrophysical Journal Supplement Series, 236, 48

Koshida S., et al., 2009, Astrophysical Journal, 700, 109

Kouzuma S., Yamaoka H., 2011, The Astrophysical Journal, 747, 12

Kozłowski S., Kochanek C. S., Ashby M. L. N., Assef R. J., Brodwin M., Eisenhardt P. R., Jannuzi B. T., Stern D., 2016, The Astrophysical Journal, 817, 119

Lacy M., et al., 2004, The Astrophysical Journal Supplement Series, Volume 154, Issue 1, pp. 166-169., 154, 166

Lacy M., Petric A., Sajina A., Canalizo G., Storrie-Lombardi L. J., Armus L., Fadda D., Marleau F. R., 2007, The Astronomical Journal, Volume 133, Issue 1, pp. 186-205., 133, 186

Landt H., Elvis M., Ward M. J., Bentz M. C., Korista K. T., Karovska M., 2011, Monthly Notices of the Royal Astronomical Society, 414, 218

Lane K. P., et al., 2007, The colour selection of distant galaxies in the UKIDSS Ultra Deep Survey Early Data Release, doi:10.1111/j.1745-3933.2007.00327.x, https://academic.oup.com/mnrasl/article-lookup/doi/10.1111/j.1745-3933.2007.00327.x

Laureijs R., et al., 2011, arXiv preprint arXiv:1110.3193

Laurent O., Mirabel I. F., Charmandaris V., Gallais P., Madden S. C., Sauvage M., Vigroux L., Cesarsky C., 2000, Astronomy and Astrophysics, 359, 887

Lawrence A., 2012, Monthly Notices of the Royal Astronomical Society, 423, 451

Lawrence A., 2018, Nature Astronomy, 2, 102

Lawrence A., Papadakis I., 1993, The Astrophysical Journal, 414, L85

Lawrence A., Watson M. G., Pounds K. A., Elvis M., 1987, Nature, 325, 694

Lawrence A., et al., 2007, Monthly Notices of the Royal Astronomical Society, 379, 1599

Lira P., Arévalo P., Uttley P., McHardy I., Breedt E., 2011, Monthly Notices of the Royal Astronomical Society, 415, 1290

Lira P., Arévalo P., Uttley P., McHardy I. M. M., Videla L., 2015, Monthly Notices of the Royal Astronomical Society, 454, 368

Lu P. K., 1977, The Astronomical Journal, 82, 773

MacLeod C. L., et al., 2010, The Astrophysical Journal, 721, 1014

MacLeod C. L., et al., 2016, Monthly Notices of the Royal Astronomical Society, 457, 389

Maltby D. T., et al., 2016, Monthly Notices of the Royal Astronomical Society: Letters, 459, L114

McCracken H. J., et al., 2012, Astronomy & Astrophysics, 544, A156

McHardy I. M., Koerding E., Knigge C., Uttley P., Fender R. P., 2006, Nature, 444, 730

McHardy I. M., et al., 2014, Monthly Notices of the Royal Astronomical Society, 444, 1469

McLure R. J., et al., 2013, Monthly Notices of the Royal Astronomical Society, 432, 2696

McLure R. J., et al., 2018, Monthly Notices of the Royal Astronomical Society, 479, 25

Mitchell J., 1784, Philosophical Transactions of the Royal Society of London, 74, 35

Molino A., et al., 2014, Monthly Notices of the Royal Astronomical Society, 441, 2891

Netzer H., 2013, The Physics and Evolution of Active Galactic Nuclei. Cambridge University Press, `https://ui.adsabs.harvard.edu/abs/2013peag.book.....N/abstract`

Neugebauer G., Soifer B. T., Matthews K., Elias ' J. H., 1989, The Astrophysical Journal, 97, 957

Oknyansky V. L., Metlova N. V., Taranova O. G., Shenavrin V. I., Artamonov B. P., Gaskell C. M., 2014, Astronomy Letters, 40, 527

Padovani P., et al., 2017, Astronomy and Astrophysics Review, 25, 2

Peach J. V., 1969, Nature, 222, 439

Pentericci L., et al., 2018, Astronomy and Astrophysics, 619

Pouliasis E., et al., 2019, Monthly Notices of the Royal Astronomical Society, 487, 4285

Richards G. T., et al., 2001, The Astronomical Journal, 121, 2308

Sánchez-Sáez P., et al., 2019, The Astrophysical Journal Supplement Series, 242, 10

Sanchez P., Lira P., Cartier R., 2016, in Active Galactic Nuclei: What's in a Name?. , doi:10.5281/ZENODO.60353

Sánchez P., et al., 2017, The Astrophysical Journal, 849, 110

Schmidt M., 1963, Nature, 197, 1040

Schmidt M., Green R. F., 1983, The Astrophysical Journal, 269, 352

Schwarzschild K., 1916, SPAW, pp 189–196

Sergeev S. G., Doroshenko V. T., Golubinskiy Y. V., Merkulova N. I., Sergeeva E. A., 2005, The Astrophysical Journal, 622, 129

Seyfert C. K., 1943, The Astrophysical Journal, 97, 28

Shappee B. J., et al., 2014, Astrophysical Journal, 788, 48

Simpson C., et al., 2012, Monthly Notices of the Royal Astronomical Society, 421, 3060

Simpson C., Westoby P., Arumugam V., Ivison R., Hartley W., Almaini O., 2013, Monthly Notices of the Royal Astronomical Society, 433, 2647

Sonnett S., Meech K., Jedicke R., Bus S., Tonry J., Hainaut O., 2013, Publications of the Astronomical Society of the Pacific, 125, 456

Stern D., et al., 2005, The Astrophysical Journal, 631, 163

Terrell J., 1967, The Astrophysical Journal, 147, 827

The Event Horizon Telescope Collaboration et al., 2019, The Astrophysical Journal Letters, 875, L1

Ueda Y., et al., 2008, The Astrophysical Journal Supplement Series, 179, 124

Uttley P., McHardy I. M., Papadakis I. E., 2002, Monthly Notices of the Royal Astronomical Society, 332, 231

Uttley P., Edelson R., McHardy I. M., Peterson B. M., Markowitz A., 2003, The Astrophysical Journal, 584, L53

Vagnetti F., Middei R., Antonucci M., Paolillo M., Serafinelli R., 2016, Astronomy & Astrophysics, 593, A55

Weedman D. W., et al., 2005, The Astrophysical Journal, 633, 706

Weymann R. J., Carswell R. F., Smith M. G., 1981, Annual Review of Astronomy and Astrophysics, 19, 41

Young M., et al., 2012, The Astrophysical Journal, 748, 124